BRISC: Annotated Dataset for Brain Tumor Segmentation and Classification with Swin-HAFNet

Amirreza Fateh[a] · Yasin Rezvani[b] · Sara Moayedi[b] · Sadjad Rezvani[b] ·
Fatemeh Fateh[c] · Mansoor Fateh[b,*] · Vahid Abolghasemi[d,*]

Abstract Accurate segmentation and classification of brain tumors from Magnetic Resonance Imaging (MRI) remain key challenges in medical image analysis, primarily due to the lack of high-quality, balanced, and diverse datasets. In this work, we present a newly developed MRI dataset named BRISC designed specifically for brain tumor segmentation and classification tasks. The dataset comprises 6,000 contrast-enhanced T1-weighted MRI scans annotated by certified radiologists and physicians. It includes three major tumor types, namely glioma, meningioma, and pituitary, as well as non-tumorous cases. Each sample includes high-resolution labels and is categorized across axial, sagittal, and coronal imaging planes to facilitate robust model development and cross-view generalization. To demonstrate the utility of the dataset, we propose a transformer-based model, leveraging a Swin Transformer backbone for multi-scale feature representation, to benchmark both segmentation and classification tasks. This model serves as a benchmark to demonstrate the utility of the BRISC dataset for advancing methodological research in neuro-oncological image analysis. datasetlink: `https://www.kaggle.com/datasets/briscdataset/brisc2025/`

[a]School of Computer Engineering, Iran University of Science and Technology (IUST), Tehran, Iran
[b]Faculty of Computer Engineering, Shahrood University of Technology, Shahrood, Iran
[c]Northern Care Alliance NHS Foundation Trust (NCA), Manchester, UK
[d]School of Computer Science and Electronic Engineering, University ofEssex, Colchester, UK
E-mail: amirreza_fateh@comp.iust.ac.ir
E-mail: yasinrezvani@shahroodut.ac.ir
E-mail: sara_moayedi@shahroodut.ac.ir
E-mail: sadjadrezvani@shahroodut.ac.ir
E-mail: fatemeh.fateh@nca.nhs.uk
E-mail: mansoor_fateh@shahroodut.ac.ir
E-mail: v.abolghasemi@essex.ac.uk
*Corresponding author

1 Introduction

Brain tumors are among the most critical medical conditions, necessitating precise and timely diagnosis for effective treatment and management [1,2]. Magnetic Resonance Imaging (MRI) plays a critical tool in diagnosing and monitoring brain tumors, owing to its non-invasive imaging capabilities and ability to provide detailed visualization of brain structures [3,4,5]. Despite significant advancements in medical imaging technologies, developing automated systems for tumor detection and segmentation remains a major challenge [6,7,8]. This challenge arises primarily from the scarcity of high-quality labeled datasets designed for these tasks. Additionally, the complexity and variability of tumor appearances across patients further complicate accurate segmentation and classification [9,10,11].

Existing brain tumor segmentation datasets, such as the Brain Tumor Segmentation (BraTS) [12], Figshare [13], and others, have significantly advanced the development of automated segmentation models. However, several limitations in these datasets drive the need for novel datasets to address emerging challenges in the field. For example, the BraTS dataset is widely used and comprehensive. However, it depends on pre-processed, standardized data that may not reflect the real-world variability in MRI acquisition protocols across institutions. Additionally, BraTS primarily focuses on gliomas and lacks representation of other tumor types, potentially limiting the generalizability of models trained on it [14,15]. The Figshare dataset, on the other hand, suffers from class imbalance and limited diversity in imaging conditions and patient demographics, which can restrict model robustness [16]. Many publicly available datasets face issues with inconsistent labeling. These inconsistencies can negatively af-

fect the training and evaluation of segmentation models [17,18,19,20]. These limitations underscore the necessity of introducing a new dataset that offers balanced class distributions, multi-institutional diversity, and high-quality expert annotations to enhance the reliability and generalizability of automated brain tumor segmentation models. Additionally, including class labels for classification tasks, such as identifying glioma, meningioma, pituitary, and non-tumorous cases, enhances the dataset's utility and supports broader real-world applications in brain tumor analysis.

To address the above challenges, we present a high-quality, well-organized brain tumor MRI dataset designed to advance research in tumor classification and segmentation. Our dataset comprises 5,000 high-resolution T1-weighted MRI images for training and 1,000 for testing, carefully selected for their suitability in visualizing brain tissue and tumor regions. Each image is accompanied by precise segmentation masks, created using advanced annotation tools and validated by radiologist and physician to ensure accuracy. The dataset focuses on three common brain tumor types called Glioma, Meningioma, and Pituitary tumors. It also includes a non-tumorous class to help models distinguish between healthy and abnormal scans. By excluding T2-weighted images and other less relevant imaging modalities, we ensure consistent data quality and minimize the risk of misclassification. An important feature of this dataset is the inclusion of multiple imaging perspectives for each tumor, covering the Coronal, Sagittal, and Axial planes. This comprehensive approach captures a diverse range of tumor characteristics, enabling researchers to train models that generalize well across different views.

In addition to introducing the dataset, we present a novel transformer-based model, Swin-HAFUNet, designed for brain tumor segmentation. This model adopts a hierarchical encoder-decoder architecture, leveraging Swin Transformer blocks to capture both local and global contextual information. It incorporates two key innovations: the Hierarchical Attention Fusion (HAF) module and the Contextual Bottleneck Enhancer (CBE). These components enhance the model's ability to aggregate multi-scale features and refine semantic representations, resulting in improved segmentation performance across diverse tumor types.

To further support diagnostic workflows, we extend the framework with a classification pipeline that automatically distinguishes between glioma, meningioma, pituitary, and non-tumorous categories. The classification branch uses multi-scale features from the Swin backbone. It combines these feature maps by reducing their dimensions, aligning their spatial sizes, and merg-

ing them, then passes them through a lightweight classification head. This design preserves both fine-grained details and high-level semantics, enabling robust tumor type discrimination alongside segmentation.

The main contributions of this work are summarized as follows:

- We introduce a large-scale, high-quality brain tumor MRI dataset with expert-annotated segmentation masks and classification labels, covering three major tumor types (glioma, meningioma, pituitary) and a non-tumorous category.
- We propose Swin-HAFUNet, a lightweight yet powerful segmentation model that integrates Swin Transformer blocks, the Hierarchical Attention Fusion (HAF) module, and the Contextual Bottleneck Enhancer (CBE) for effective multi-scale feature integration.
- We develop an efficient classification pipeline that leverages the Swin backbone's features through dimension reduction and fusion, achieving accurate tumor type diagnosis.
- Extensive experiments demonstrate that our model outperforms existing state-of-the-art methods in brain tumor segmentation and classification.

2 Related Work

In recent years, significant advancements in deep learning have driven the development of automated brain tumor diagnosis systems. A key factor in achieving high-performing models is the availability of high-quality annotated datasets, which serve as a foundation for both segmentation and classification tasks. Numerous brain tumor datasets have been introduced, each varying in imaging modalities, annotation quality, tumor types, and overall dataset size. This section reviews existing brain tumor datasets in detail. We organize them by their primary purpose, either segmentation or classification, and analyze their key features, advantages, and limitations. By examining these datasets, we aim to underscore the challenges they present and justify the need for introducing our novel dataset with refined annotations and enhanced diagnostic utility.

2.1 Segmentation

When addressing brain MRI segmentation, the BraTS challenge remains a pivotal benchmark in the field [12]. raTS receives annual updates and has evolved significantly. Its latest version includes diverse tumor types such as gliomas, pediatric brain tumors, and brain

metastases [21]. While BraTS provides high-quality multimodal MRI data and expert-annotated tumor sub-regions, it predominantly emphasizes cases with multiple MRI sequences, such as T1, T2, T1-contrast, and FLAIR. This focus may not fully reflect real-world clinical scenarios where single-sequence scans are more commonly encountered. Additionally, BraTS' reliance on synthetic modalities for specific cases introduces variability that might not always correlate with actual clinical imaging conditions. These limitations underscore the need for complementary datasets that encompass a broader range of imaging scenarios and real-world variability.

Another notable dataset in brain tumor segmentation is the Medical Segmentation Decathlon (MSD) [22]. Unlike the original BraTS challenge, which primarily targets gliomas, MSD encompasses a broader spectrum of medical imaging tasks, including brain tumor segmentation. The brain MRI data in MSD originates from multiple medical centers, enhancing the dataset's heterogeneity and, consequently, the potential generalizability of models trained on it. However, this multi-center nature introduces variability in imaging protocols, scanner types, and acquisition parameters, complicating model training and evaluation.

In addition to BraTS and MSD, the Federated Tumor Segmentation (FeTS) dataset [23] represents another key resource in brain tumor segmentation. FeTS builds upon the BraTS dataset while incorporating additional clinical data from multiple healthcare institutions. It primarily focuses on gliomas, with multimodal MRI scans meticulously annotated by expert radiologists and physicians. The inclusion of multi-center data enhances the generalizability of models developed using FeTS. However, FeTS is predominantly centered on glioma cases, limiting its applicability to other tumor types, such as meningiomas and pituitary tumors. This narrow scope highlights the need for datasets that comprehensively cover a wider variety of brain tumor types for more generalized segmentation tasks.

Beyond BraTS, MSD, and FeTS, several other datasets contribute to advancing brain MRI segmentation. BrainMetShare [24] is one such dataset, comprising 156 whole-brain MRI studies with high-resolution, multi-modal pre- and post-contrast sequences from patients presenting with at least one brain metastasis. Ground-truth segmentations provided by expert radiologists and physicians accompany each study, making it a valuable resource for developing models tailored to brain metastases. Unlike glioma-focused datasets, BrainMetShare's emphasis on metastatic brain tumors offers a complementary perspective, addressing an important clinical need.

The Open Access Series of Imaging Studies (OASIS) project [25] also provides a significant resource for brain MRI research. While not explicitly designed for tumor segmentation, OASIS offers a large-scale collection of multimodal brain MRI scans, including longitudinal data from healthy individuals and patients with various neurological disorders. OASIS-3, in particular, features structural MRI scans acquired over time, enabling the study of disease progression. Although primarily intended for neuroscience research, OASIS' comprehensive data can be leveraged for developing segmentation models that generalize across different brain conditions, including tumors.

Another valuable initiative is fastMRI, spearheaded by Facebook AI Research and NYU Langone Health [26]. While the primary objective of fastMRI is to promote advancements in MRI reconstruction, the dataset includes a substantial number of fully sampled brain MRI scans acquired on 1.5T and 3T scanners. These high-resolution scans, encompassing T1-weighted, T2-weighted, and FLAIR sequences, can be repurposed for segmentation tasks. The large scale and high diversity of the fastMRI dataset make it a valuable resource for training robust models, particularly in scenarios where high-quality input data is critical.

The LGG Segmentation Dataset [27], available on Kaggle, specifically targets lower-grade gliomas by providing brain MRI scans alongside manual FLAIR abnormality segmentation masks. This dataset addresses a gap by offering focused data for a specific tumor grade, enabling the development of models tailored to low-grade glioma segmentation. Although limited in scope, its accessibility and detailed annotations make it a popular choice for researchers developing segmentation algorithms for lower-grade gliomas.

2.2 Classifcation

The development of robust brain tumor classification models heavily relies on high-quality datasets that provide diverse and well-annotated medical imaging data. Several publicly available datasets have been widely used in recent research, enabling the training and evaluation of deep learning models for brain tumor classification. These datasets vary in size, imaging modalities, and tumor types, offering researchers a range of options for developing and benchmarking their models.

One of the most widely used datasets is the Figshare [13], which contains 3,064 T1-weighted contrast-enhanced MRI (CE-MRI) images categorized into three tumor types: glioma, meningioma, and pituitary tumors. This dataset has been instrumental in advancing

brain tumor classification research. It provides a balanced distribution of tumor types, making it suitable for multi-class classification tasks. The dataset's accessibility and comprehensive annotations have made it a benchmark for evaluating the performance of deep learning models, as demonstrated in studies such as Islam et al. [28] and Balamurugan et al. [29].

Another notable dataset is one of the Kaggle Brain Tumor MRI datasets, introduced by Nickparvar [30], which includes 7,023 brain MRI images categorized into four classes: glioma, meningioma, pituitary tumors, and non-tumorous. This dataset is particularly valuable for its diversity and inclusion of non-tumor cases, allowing researchers to develop models capable of distinguishing between healthy and pathological brain scans. The dataset has been used in studies such as Chen et al. [31] and Alanazi et al. [32], where it facilitated the development of transfer learning and feature fusion approaches for brain tumor classification.

As previously discussed, the BraTS dataset [12] is also commonly repurposed for classification tasks, leveraging its multi-modal MRI data (T1, T1c, T2, FLAIR). The BraTS dataset has been used in studies such as Ghosal et al. [33], where researchers developed a Squeeze and Excitation ResNet model for brain tumor classification, achieving an accuracy of 93.83%. The dataset's multi-modal nature allows for the exploration of complementary information from different imaging modalities, enhancing model performance.

The "Brain Tumor" dataset [34] is another valuable resource, providing a collection of brain MRI images with annotations for various tumor types. The dataset's inclusion of rare tumor types and diverse imaging protocols makes it a valuable resource for developing models that can generalize across different clinical settings.

In summary, the availability of diverse and well-annotated datasets has been instrumental in advancing brain tumor classification research. These datasets continue to play a critical role in driving innovation in the field, providing the foundation for future research and clinical applications. However, despite the progress made, there is still a pressing need for new datasets that address specific challenges, such as the inclusion of rare tumor types, multi-modal imaging data, and more diverse patient demographics. Additionally, existing datasets often focus on either segmentation or classification tasks, limiting their utility for models that require simultaneous learning of both tasks. The introduction of a new dataset that supports both segmentation and classification tasks can bridge this gap, providing a more comprehensive resource for training and evaluating models. Such datasets can also incorporate advanced annotations, such as tumor sub-regions

and molecular markers, which are critical for developing models that align with clinical needs. These datasets continue to play a critical role in driving innovation in the field, providing the foundation for future research and clinical applications.

3 Background & Summary

3.1 Overview of Brain Tumors

Brain tumours are amongst the most fatal of all cancers [35]. Amongst paediatric solid tumours, brain tumours are most fatal and commonly occurring [35]. There is diversity in the types of brain tumours, including but not limited to gliomas which account for 45% of brain tumours with pituitary tumours and meningiomas accounting for 15% each [36]. The gold standard imaging for diagnosis of a brain tumours or brain metastases is an MRI scan with gadolinium [37]. When possible, management is initially via surgery to remove the lesion which is then sent for histological and molecular genotype identification [37]. Pre, intra and post-operative MRIs can be used to guide surgical resection and management [37,38,39]. Intra-operatively, functional MRIs visualise cerebrovascular activity which can be correlated with neuronal activity, aiding the surgical team. Other techniques such as cord simulation can also be used [38]. In many scenarios, regardless of skill, neurosurgical reach has to be limited for safety due to the presence of many functionally important regions within the organ [35,37]. Further management includes the use of medical interventions for symptomatic management, radiotherapy and chemotherapy [35]. The blood brain barrier poses challenges to medical interventions and chemotherapy, this barrier filters material entering the brain via circulation, limiting medical access to the brain [35]. Localisation of the lesion and adjacent structures via MRIs can guide both surgical and radiotherapeutic planning [40]. In summary, MRI scans are used in the initial diagnosis and management planning of brain tumours, including pre-surgical use and as guidance for radiotherapy [40].

3.1.1 Glioma

Gliomas are primary brain tumours, they are the most common of malignant primary brain tumours in adults [37]. They arise from glial cells or stem cells which develop glial properties during neoplastic changes [41]. Glial cells designate a group of different cells which provide support for neurons, for example by the formation of axonal myelin sheaths [42]. For adults, the most aggressive form of gliomas, the glioblastoma, has a two

year prognosis [35]. Gliomas can be typed against the WHO 2016 classification of CNS tumours [41].

Diffuse forms of gliomas can grow in irregular shapes, extensively infiltrating brain parenchyma [41], this makes neurosurgical management difficult as safe maintenance of functional brain tissue is required during resection [35, 37].

3.1.2 Meningioma

Meningiomas in adults are the most common, being 30% of central nervous system tumours, whilst they are rare amongst children [43]. They arise from cells on the outer layer of the arachnoid mater, a part of the meninges [43]. The meninges is a layer in the central nervous system which encompasses the brain, cerebrospinal fluid and spinal cord [44]. Though, a meningioma could arise anywhere on the meninges, 98% of meningiomas are intracranial [43]. Usually benign lesions, they can be slow growing [43]. MRI scans in conjunction with CT scan can be sued for diagnosis and treatment planning [43]. Treatment generally consists of neurosurgical treatment, occasionally in adjunct with radiotherapy [43]. Benign meningiomas can grow to a large size with pressures on the brain causing symptoms [45]. Non-benign meningiomas are associated with irregular shapes and tumours heterogeneity and therefore, benign meningiomas tend to be associated with regular shapes and homogeneity [46].

3.1.3 Pituitary Tumors

These are tumours originating in the pituitary gland, a small structure at the base of the brain, above the sphenoid bone [47]. The pituitary gland has an essential role in growth, metabolism and reproduction [48]. Due to this, pituitary tumours can cause a wide range of symptoms including but not limited to; mood disorders, diabetes mellitus, obesity, infertility and visual disturbances [48]. However, only one third of these tumours are symptomatic [48]. The majority of pituitary tumours are benign and when treated, treatment generally includes neurosurgical resection and radiotherapy [49].

3.1.4 Non-Tumorous Conditions

There are space occupying lesions which are non tumorous in nature, they can be inflammatory, like infections, or arise from vascular abnormalities. Some examples of such space occupying lesions include abscesses, cysts, haematomas and aneurysms [50]. Due to its high soft tissue sensitivity, MRIs can be used to aid characterisation of space occupying lesions, though surgical biopsy may still be required to finalise results [51].

3.2 Magnetic resonance imaging of human brain

3.2.1 Anatomical planes

The main anatomical planes are coronal, transverse and sagittal planes [52]. These may be more simply described as a 'front to back' vertical plane, a 'top to bottom' horizontal plane, a longitudinal 'side to side' plane [52]. For a radiologist reporting an MRI scan, the above planes are available for viewing [53].

3.3 MRI Basics

3.3.1 MRI scans

Magnetic resonance imaging uses non hazardous electromagnetic radiation to provide images of the body's internal structure [54]. A computer constructs images from the information gathered by the MR scanner [54]. These images can be viewed in sequential 2D 'slices' and can also be used to develop a 3D image [54]. There are two main types of images usually provided, T1 weighted and T2 weighted images [54].

3.3.2 T1-Weighted Imaging

This form of imaging fat is displayed brightly, therefore it can provide detailed anatomical images of soft tissues especially in the brain [54].

3.3.3 T2-Weighted Imaging

In this format, the image represents water, such as CSF, brightly [54], due to this they can be used to detect inflammation [54] and aid distinguish tumours from other space occupying lesions [54]. Most of the diagnostics for space occupying lesions can be done using these two imaging modalities [55].

3.3.4 Further modalities

Further MRI modalities are used by radiologists in conjunction with T1 and T2-weighted imaging to aid space occupying lesion diagnostics, these include

perfusion-weighted imaging, diffusion-weighted imaging, MR spectroscopy [55] and FLAIR [56]. A radiologist generally has access to the full range of slices and may have further imaging modalities to aid diagnostic reasoning.

3.4 Challenges in Brain Tumor Diagnosis

3.4.1 Misdiagnosis Risks

As mentioned above, some tumours do not cause symptoms until reaching a certain growth [45], this may lead to late clinical suspicion to warrant imaging. When available and possible, the best imaging modality are MRI scans [37]. Even the use of neurological imaging can lead to misdiagnosis as neoplastic and non neoplastic conditions can mimic each other. As mentioned above, there are non tumorous space occupying lesions, these can be benign, meaning surgical resection and biopsy exposes many patients unnecessarily to the risks of surgery [57]. There are also neoplastic brain lesions which do not appear as a space occupying lesion [57]. Not neglecting T1 precontrast imaging can aid avoidance of misdiagnosis [57]. Further MR imaging modalities and a thorough clinical assessment alongside some further investigations can aid in reducing errors [57]. There are certain tumours which are difficult to visualised on MRI, though MRIs provide a high level of diagnostic accuracy for most tumours [58].

4 Methods

4.1 Dataset Overview

The BRain tumor Image Segmentation and Classification (BRISC) dataset has been meticulously curated to address key challenges in brain tumor research, particularly in the domains of segmentation and classification tasks. It provides a balanced, high-quality collection of MRI data, annotated for both research and clinical applications. The dataset includes images with labels for four categories: Glioma, Meningioma, Pituitary tumors, and non-tumorous. By focusing on comprehensive data collection and rigorous annotation processes, the dataset aims to advance the development of robust machine learning models in medical imaging.

4.2 Purpose and Objectives

The primary goal of collecting and releasing this dataset is to overcome limitations observed in existing brain tumor datasets, such as class imbalance, lack of diversity, and annotation inconsistencies. While datasets like BraTS have driven significant advancements in glioma segmentation, their exclusive focus on gliomas and reliance on pre-processed data limit their generalizability to other tumor types and real-world scenarios. Our dataset expands the scope by incorporating multiple tumor types and includes a "non-tumorous" class to aid in broader diagnostic tasks. This addition makes the dataset highly versatile, enabling its use in applications ranging from multi-class tumor classification to binary tumor detection. The key objectives include:

1. Supporting segmentation tasks by providing accurate tumor masks.
2. Facilitating multi-class classification through balanced representation of tumor types.

4.3 Dataset Composition and Planar Distributions

The dataset comprises 6,000 MRI images, divided into training and testing sets, as detailed in Table 1. This structured division ensures robust evaluation metrics while providing ample data for training advanced machine learning models. For the training dataset, the total number of images across the planes is 5,000, and for testing, the total is 1,000.

In addition to the class-based distribution, we provide another form of distribution, which is dataset composition by MRI planes. This breakdown categorizes images into Coronal, Sagittal, and Axial planes, helping to analyze how different orientations are represented in the dataset. As shown in Table 2, the distribution of different MRI planes is nearly uniform, similar to the distribution of different classes in Table 1. This balanced distribution ensures that no particular class or plane is overrepresented, which is crucial for preventing model bias and improving generalization.

4.4 Data Source and Preprocessing

This dataset was derived from "Brain Tumor MRI Dataset" [59] that combined data from three prominent sources: Figshare [13], SARTAJ [60], and Br35H [61]. The original dataset included 7,023 MRI images across four classes: Glioma, Meningioma, non-tumorous, and Pituitary. The "non-tumorous" class images were specifically sourced from the Br35H dataset. During preprocessing, several steps were undertaken to ensure the quality and consistency of our final dataset:

– **Separation of T1 Images**: Only T1-weighted MRI images were retained to maintain uniformity in imaging modality.

Table 1: Class distribution in the training and testing parts of BRISC

Class	Training Images	Testing Images	Total Images
Glioma	1,147	254	1,401
Meningioma	1,329	306	1,635
Pituitary	1,457	300	1,757
non-tumorous	1,067	140	1,207
Total	**5,000**	**1,000**	**6,000**

Table 2: Class distribution based on MRI planes in the training and testing parts of BRISC

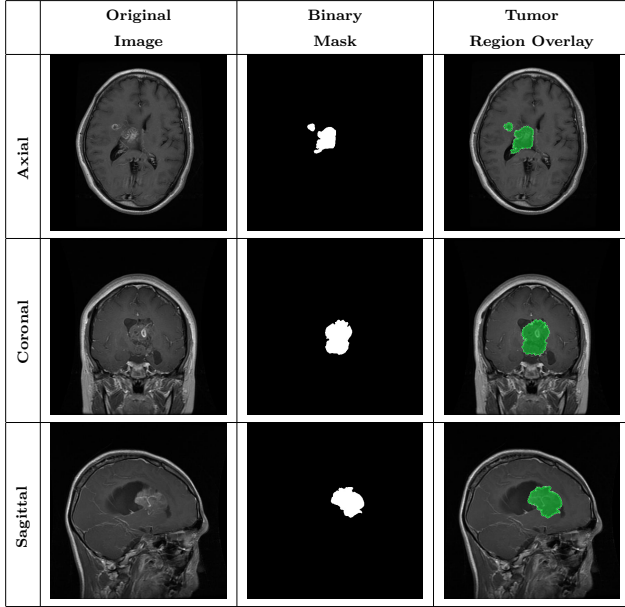| Class\Plane	Train			Test		
	Axial	Coronal	Sagittal	Axial	Coronal	Sagittal
Glioma	347	428	372	85	81	88
Meningioma	423	426	480	134	89	83
Pituitary	428	496	533	116	98	86
non-tumorous	352	310	405	52	48	40
Total per plane	1550	1660	1790	387	316	297
Total	**5000**			**1000**		

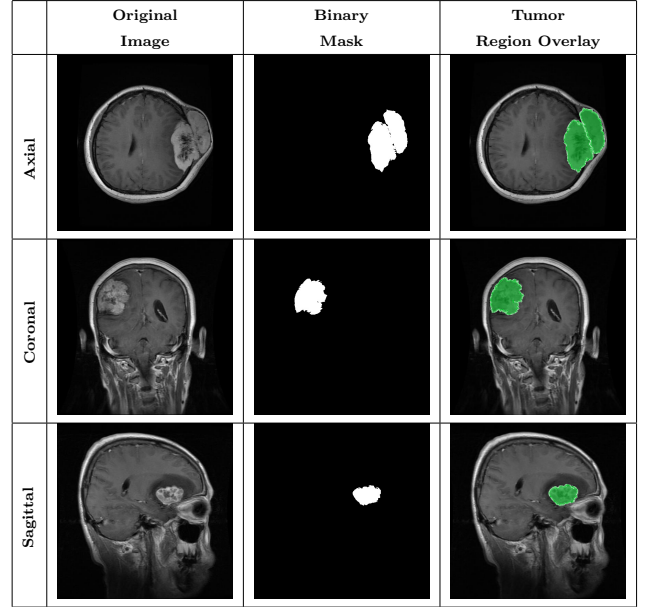Fig. 1: Samples of Glioma segmentation across different imaging planes

Fig. 2: Samples of Meningioma segmentation across different imaging planes

– **Quality Control**: Images with incorrect or inconsistent labels were identified and removed with the assistance of radiologist and physician.
– **Standardization**: Images were resized and margins were adjusted to improve model accuracy during training.

4.5 Imaging Details

All images in the dataset are T1-weighted contrast-enhanced MRI scans, selected specifically from the "Brain Tumor MRI Dataset" (Kaggle) [59]. Although the original dataset included some T2-weighted images,
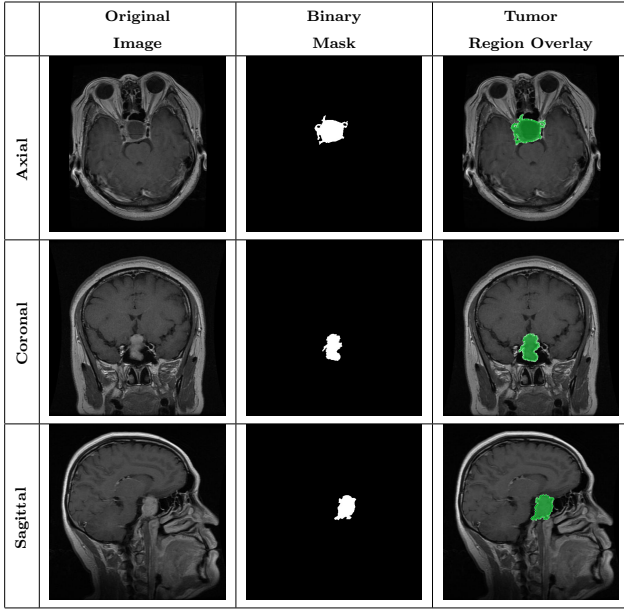
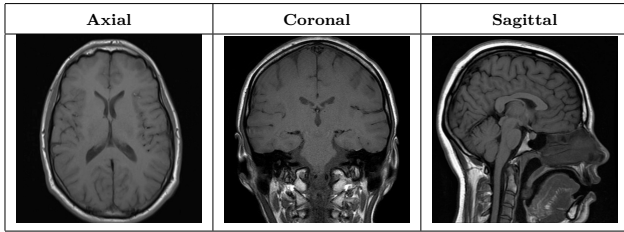Fig. 3: Samples of Pituitary segmentation across different imaging planes

Fig. 4: Samples of non-tumorous across different imaging planes

we exclusively selected T1-weighted scans for their superior ability to highlight tumor boundaries effectively. Another notable characteristic of this dataset is the length of MRI sequences. While typical brain MRI studies often consist of longer sequences, the majority of sequences in this dataset were notably short, ranging from 1 to 5 images per sequence. Sequences with only one image were excluded, as even experienced radiologists and physicians found it challenging to identify tumors accurately in these cases.

4.6 Annotation Process

The dataset underwent a meticulous annotation and review process to ensure accuracy and reliability. Annotation was performed using the AnyLabeling tool [62], which facilitated efficient and precise delineation of tumor regions. Each image was reviewed and edited multi-
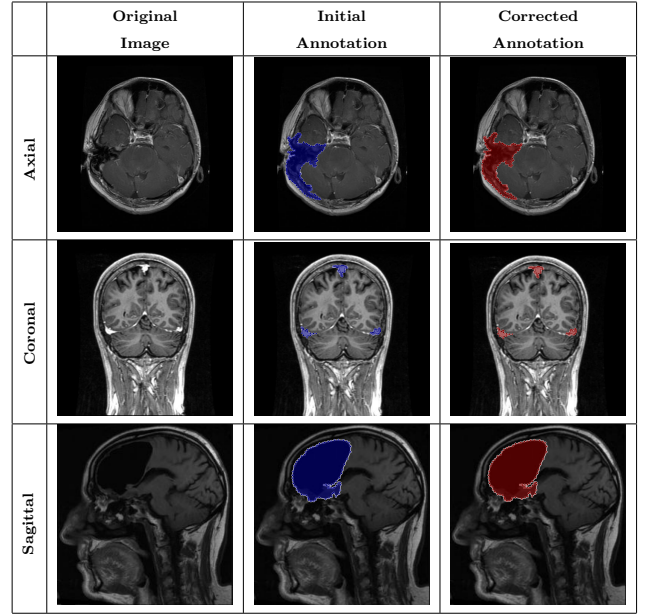

Fig. 5: Samples of whole-region misannotations. The red area indicates regions that were initially marked as tumors but were identified by radiologist and physician as non-tumorous.

ple times with the input of a certified physician and radiologist. Key steps in the annotation process included:

– **Tumor Mask Refinement**: Using AnyLabeling [62], points of interest for tumors were iteratively refined to ensure precise segmentation masks.
– **Class Correction**: Images incorrectly classified as "non-tumorous" in the original dataset were re-evaluated and removed from this class if necessary.
– **Consensus Reviews**: Discrepancies in annotation were resolved collaboratively by the physician and radiologist.

4.7 Visual Demonstrations of the Dataset

This section provides an in-depth exploration of the dataset through visual examples and analytical discussions, illustrating its structure, composition, and inherent challenges. These demonstrations aim to deepen understanding of the dataset's unique features while highlighting its potential applications in advanced segmentation and classification tasks.

4.7.1 Overview of Classes

The dataset encompasses four distinct classes: "Glioma", "Meningioma", "Pituitary" tumors, and
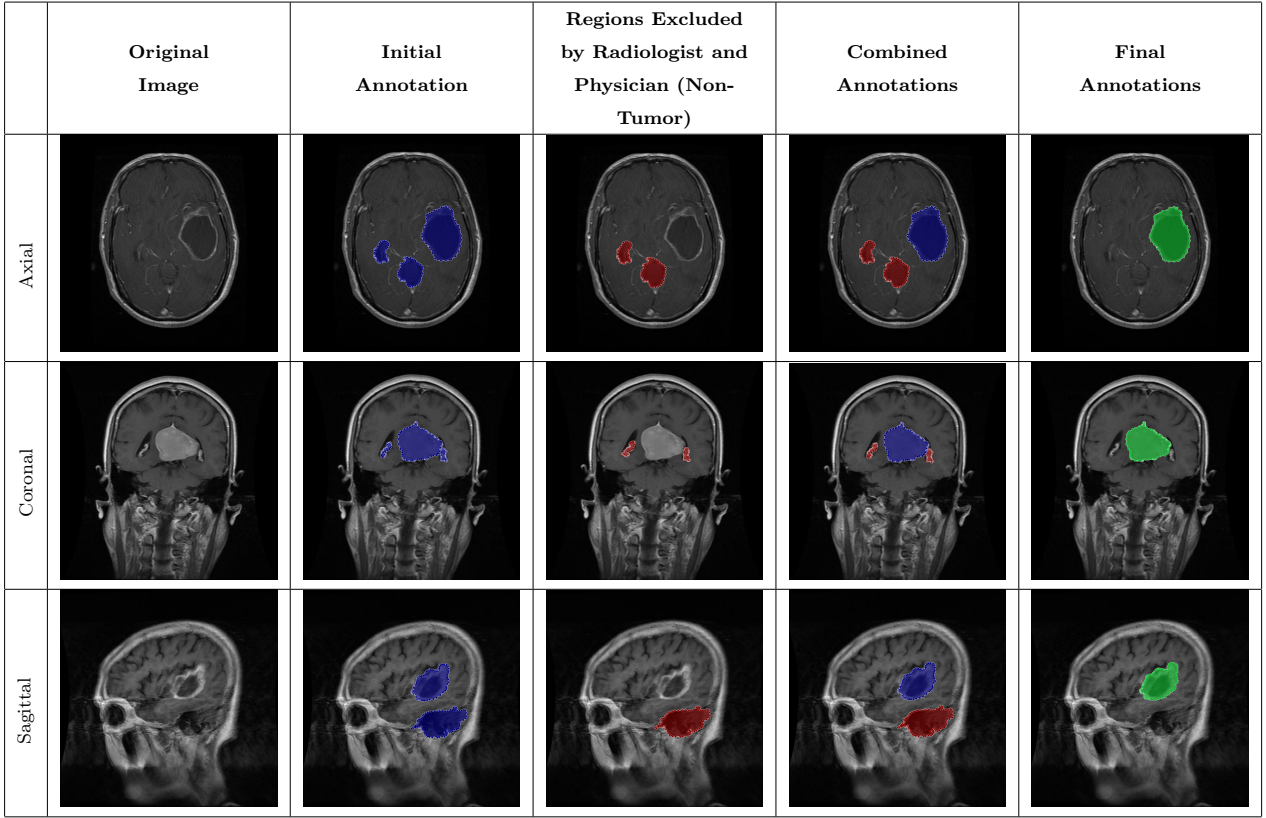
Fig. 6: Samples of partial-region overannotations. The red area indicates regions that were initially marked as tumorous but were later identified by the radiologist and physician as non-tumorous.

"non-tumorous". As detailed in Section 3.1, each class presents unique characteristics and complexities. This subsection offers representative visual examples from each class, including raw MRI scans alongside their annotated tumor masks, emphasizing the diversity and precision of the dataset.

–   **Glioma**: Gliomas are irregularly shaped and often infiltrate surrounding tissues, presenting significant challenges for precise boundary definition. These complexities require robust segmentation techniques to capture their variable morphology. As shown in Figure 1, gliomas exhibit irregular and diffuse growth patterns, which are highlighted through annotated tumor masks.

–   **Meningioma**: Meningiomas are generally well-circumscribed and homogeneous, making them easier to segment. However, their proximity to sensitive regions such as the meninges can complicate diagnostic tasks. An example of a meningioma and its segmentation mask is presented in Figure 2, illustrating the clarity of its boundaries.

–   **Pituitary Tumors**: Located at the base of the brain near critical structures like the optic chiasm, pituitary tumors demand careful delineation to avoid diagnostic errors. As shown in Figure 3, the segmentation accurately captures the tumor's boundaries without encroaching on adjacent critical regions.

–   **non-tumorous**: This control class is integral for training models to distinguish healthy scans from those with abnormalities. Including "non-tumorous" cases enhances the dataset's robustness for binary and multi-class classification. Figure 4 illustrates an example of a healthy brain scan with no abnormalities.

4.7.2 Tumor Mask and Annotation Quality

Achieving accurate tumor segmentation required a meticulous process of iterative reviews and refinements, conducted in close collaboration with a physician and a radiologist. This collaborative effort was crucial in ensuring that the final annotations accurately reflected the true tumor boundaries, minimizing errors and improving the overall quality of the dataset.
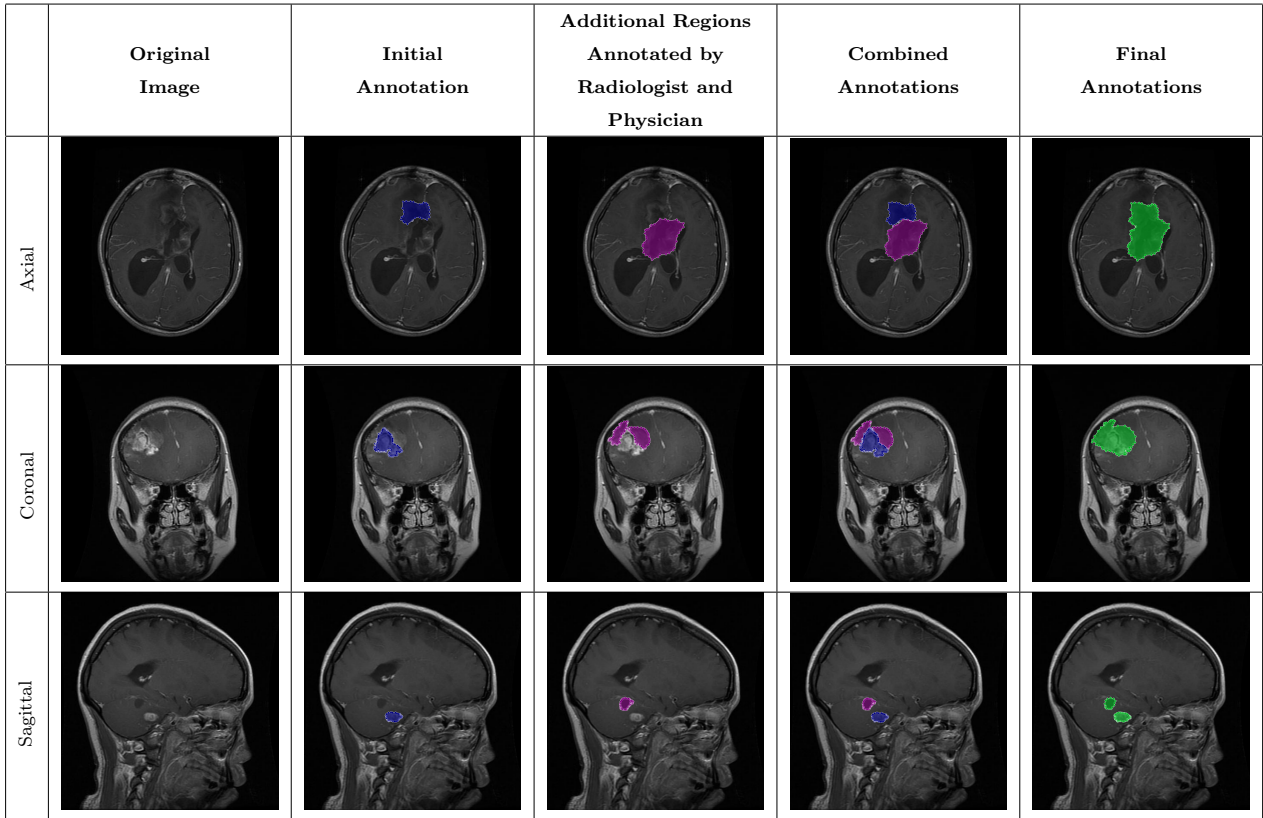
Fig. 7: Samples of partial-region underannotations. The purple area indicates regions that were initially marked as non-tumorous but were later identified by the radiologist and physician as tumorous.

In some cases, regions initially annotated as tumors were later identified by physician and radiologist as non-tumorous. These corrections were essential to avoid false positives that could mislead model training. An example of such a case is shown in Figure 5, where an area initially believed to be a tumor was excluded from the final annotation after expert review.

In other instances, certain areas that were mistakenly included as part of the tumor region were refined based on radiologist and physician feedback. These areas, though visually similar to tumor tissue, were determined to be non-tumorous upon closer examination. As illustrated in Figure 6, the removal of these incorrect segments resulted in more precise tumor masks and enhanced the reliability of the dataset.

Conversely, there were cases where genuine tumor regions had been overlooked during the initial annotation process. With input from the Physician and radiologist, these missing regions were added to the annotations, ensuring that the masks comprehensively captured all tumor areas. Figure 7 demonstrates an example of such an adjustment, where previously unannotated tumor segments were correctly incorporated into the final mask.

4.7.3 Challenges of non-tumorous Conditions

Non-tumorous conditions frequently mimic tumors in MRI scans, posing significant challenges not only for classification tasks but also for segmentation. This section visualizes examples of these conditions and compares them with actual tumors to highlight their distinctions.

Brain lesions, for instance, often resemble tumors both in shape and intensity. These similarities can lead to misclassification as well as erroneous segmentation of the lesion as a tumor. Cysts are another condition that can complicate both segmentation and classification. Typically fluid-filled and round, cysts may be mistaken for tumors during segmentation tasks due to their well-defined boundaries. Calcifications, which appear as bright regions on MRI scans, can similarly lead to errors in both classification and segmentation. While their growth patterns differ from tumors, their intensity can cause segmentation models to incorrectly label them as tumorous regions.

These challenges underscore the critical importance of radiologist and physician expertise in ensuring accurate segmentation and classification of such conditions.

The examples provided highlight the need for robust models capable of distinguishing these non-tumorous conditions from actual tumors in both classification and segmentation tasks.

5 Proposed method

5.1 Segmentation task

5.1.1 Overview

Although the original dataset was designed primarily for classification tasks, through close collaboration with physicians and radiologists, we have extended it by providing high-quality expert annotations delineating tumor regions, thereby creating a new segmentation benchmark. In this part, we present a novel transformer-based architecture for accurate and efficient tumor segmentation in brain MRI scans. The overall framework adopts an encoder-decoder structure, where the encoder extracts multi-scale semantic representations from the input image, and the decoder progressively reconstructs the segmentation map using enhanced contextual features.

The encoder is built upon a hierarchical Swin Transformer backbone, which efficiently captures both local and global dependencies through shifted window-based self-attention. To further refine the extracted features, we use the Contextual Bottleneck Enhancer (CBE), which enriches feature representations using a sequence of lightweight yet effective operations, including shifted multilayer perceptrons (MLPs) and gated encoding units.

To preserve high-resolution semantic details during decoding, we design a lightweight decoder that includes Adaptive Context Aggregator blocks, which adaptively fuse local and global context from the encoder outputs. Additionally, we propose a Hierarchical Attention Fusion (HAF) module that integrates multi-scale features from different encoder levels through a combination of Swin Transformer blocks and deformable convolutions, allowing the model to capture hierarchical dependencies and spatial variations effectively.

Together, these components enable our model to achieve robust segmentation performance while maintaining computational efficiency. The complete architecture is illustrated in Figure 8.

5.1.2 Encoder Architecture

The encoder of the proposed segmentation model is designed to extract rich hierarchical features from brain MRI scans using a multi-stage Swin Transformer-based backbone. It begins with a *patch partition* module, which splits the input image into non-overlapping patches. These patches are then flattened and mapped to a fixed-dimensional embedding space through a Linear Embedding layer.

Following this, the encoder comprises three repeated stages, each consisting of two Swin Transformer Blocks followed by a *patch merging* layer. The Swin Transformer blocks utilize a window-based self-attention mechanism with a shifted window strategy, allowing the model to effectively capture local and non-local dependencies with reduced computational cost. The patch merging operation downsamples the spatial resolution while increasing the feature dimensionality, forming a hierarchical representation.

This hierarchical structure enables the encoder to progressively capture multi-scale semantic information, which is crucial for segmenting tumors of varying sizes and shapes. The feature maps from different stages are later passed to the HAF modules, enabling multi-level feature interaction and refinement in the decoding process.

5.1.3 Hierarchical Attention Fusion (HAF) Module

The HAF module is designed to effectively integrate encoder and decoder features at each resolution level, enhancing the model's capacity to capture both low-level spatial detail and high-level semantic context.

At each stage of the decoder, the HAF module takes two inputs:

- x_{skip}: The skip connection feature map from the encoder.
- x_{decoder}: the upsampled feature map from the previous decoder layer.

The decoder feature x_{decoder} is first passed through a *Swin Transformer Block* to refine contextual dependencies and enhance representation. As shown in Equation 1, the refined feature is then concatenated with the corresponding encoder feature x_{skip} along the channel dimension.

$$x_{\text{cat}} = \text{Concat}(x_{\text{skip}}, \ \text{Swin}(x_{\text{decoder}})) \qquad (1)$$

This concatenated feature map x_{cat} is then projected through a 1×1 convolutional layer (Equation 2).

$$x_{\text{out}} = \text{Conv}_{1\times1}(x_{\text{cat}}) \qquad (2)$$

The resulting output x_{out} maintains the same spatial resolution as x_{decoder} and serves as the input for the next step in the decoder. This fusion strategy allows
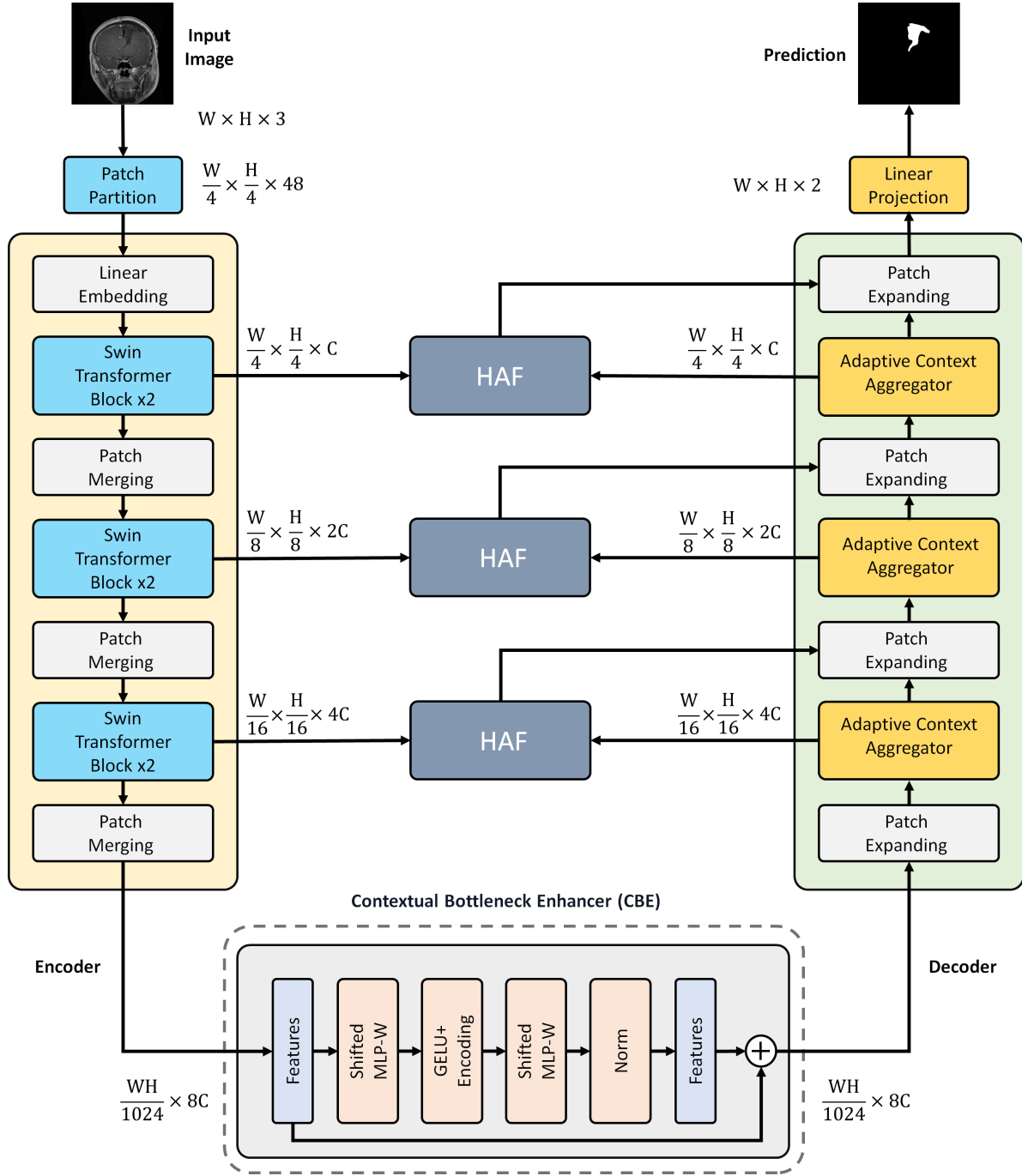
Fig. 8: The overview of the Swin-HAFUNet

the network to maintain fine spatial information while enriching the semantic features through transformer-based attention. The Architecture of HAF is shown in Figure 9.

5.1.4 Contextual Bottleneck Enhancer (CBE)

The CBE employs a Tokenized MLP Block to enhance feature representations efficiently at the bottle-

neck stage. This module captures long-range dependencies while maintaining computational efficiency.

The process begins with a spatial shift along the width axis, followed by a linear projection to produce token embeddings. These tokens pass through a shifted MLP layer (across width), then through a depth-wise convolution and GELU activation, which introduces non-linearity and encodes positional information. The
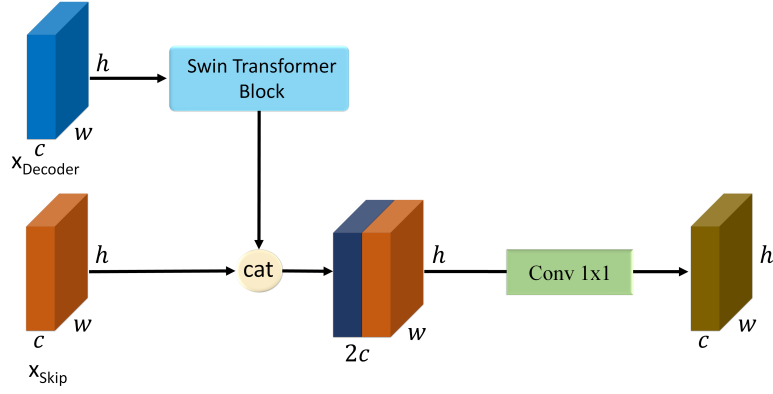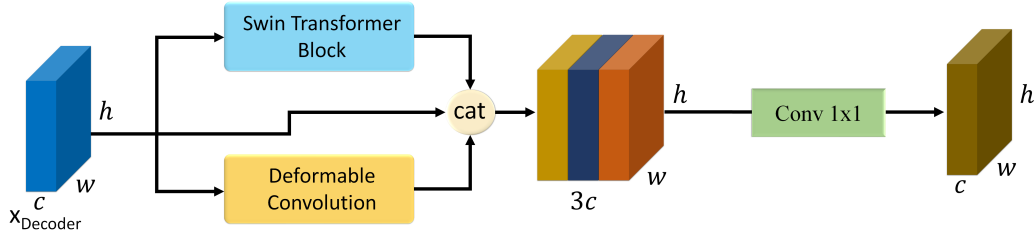
Fig. 9: Hierarchical Attention Fusion module

Fig. 10: Structure of the Adaptive Context Aggregator module.

output is then processed by another shifted MLP along the height axis.

A residual connection adds the original input tokens to the output of the second MLP, and the result is normalized using Layer Normalization (LN). This sequence can be summarized in Equation 3.

1. $\quad X_{\text{shift}}^W = \text{Shift}_W(X)$
2. $\quad\quad T_W = \text{MLP}_W(X_{\text{shift}}^W)$
3. $\quad\quad\quad Y = \text{GELU}(\text{DWConv}(T_W))$
4. $\quad\quad Y_{\text{shift}}^H = \text{Shift}_H(Y)$
5. $\quad\quad\quad T_H = \text{MLP}_H(Y_{\text{shift}}^H)$
6. $\quad\quad\quad Z = \text{LN}(T_H + T)$

$$(3)$$

where T represents the original tokenized input. This design enables the block to model spatial context in both directions and fuse the information effectively via residual learning.

This block structure is adapted with modifications from the tokenized MLP design presented in [63], but tailored to our segmentation task.

5.1.5 Decoder Architecture

The decoder receives as input the enhanced representation produced by CBE and gradually reconstructs

the segmentation map through a hierarchical upsampling process. Unlike traditional encoder-decoder architectures, our decoder integrates semantic context at multiple levels by leveraging the Adaptive Context Aggregator and HAF module.

At each stage of the decoder, the feature map undergoes a Patch Expanding operation to increase the spatial resolution. Following this, contextual features generated by the Adaptive Context Aggregator are fused with encoder features using the HAF module. The output of the HAF block serves as an enhanced skip connection, injected into the decoder pathway to guide the reconstruction process with both fine-grained and semantic details.

This structured design ensures that skip connections are not merely concatenations of encoder features, but rather semantically enriched representations aligned with the decoder's current context. After multiple stages of patch expansion and fusion, the final feature map is passed through a linear projection layer to produce the segmentation output. culminating in a final linear projection to generate the final prediction map.

5.1.6 Adaptive Context Aggregator

To effectively inject adaptive context into the decoder path, we employ the Adaptive Context Aggregator module. This block is responsible for enhancing the de-

coder features by integrating both local geometric and global semantic information.

As illustrated in Figure 10, the Adaptive Context Aggregator module receives the decoder feature map as input. It first processes this input through a Swin Transformer Block to capture long-range dependencies and global contextual cues. In parallel, the same input is passed through a Deformable Convolution layer to focus on important local structures and spatially variant patterns.

The outputs of both the Swin Transformer and the Deformable Convolution branches are concatenated and fused via a 1×1 convolution layer. This fusion ensures that both global and local contexts are adaptively aggregated in a computationally efficient manner. The resulting feature map serves two purposes: it is passed to the HAF module to refine the skip connection at the current decoder level, and it is also forwarded to the subsequent Patch Expanding block in the decoder pipeline. This dual role ensures both better feature fusion and more informed upsampling in the reconstruction process.

5.2 Classification task

5.2.1 Overview

In addition to tumor segmentation, we further design a classification pipeline to automatically discriminate between four diagnostic categories: *glioma*, *meningioma*, *pituitary*, and *non-tumorous*. The classification branch exploits the multi-scale feature representations extracted by the Swin Transformer backbone and processes them through a sequence of dimension and spatial reduction steps, followed by feature fusion and a lightweight classification head. The goal of this design is to unify heterogeneous multi-scale features into a compact representation that preserves both local and global discriminative cues, enabling robust classification of brain tumor types. The overall structure of the classification framework is illustrated in Figure 11.

5.2.2 Backbone Architecture

The classification framework employs the Swin Transformer backbone, which naturally produces multi-scale feature representations through its hierarchical design. The backbone makes features at four progressive stages, capturing both fine spatial details in early layers and high-level semantic patterns in deeper layers. This multi-scale approach is particularly valuable for tumor classification, where diagnostic decisions depend

on both localized texture features and global anatomical context.

5.2.3 Dimension Reduction

Each feature map $\mathbf{F}_i \in \mathbb{R}^{C_i \times H_i \times W_i}$ is first passed through a 1×1 convolution to reduce the channel dimension to 64. This projection ensures uniform channel size and reduces computational overhead. as shown in Equation 4 the operation is followed by a ReLU activation and Batch Normalization (BN) to improve representation stability and training convergence.

$$\mathbf{F}'_i = \mathrm{BN}\big(\sigma(\mathrm{Conv}_{1\times1}(\mathbf{F}_i))\big), \quad \mathbf{F}'_i \in \mathbb{R}^{64 \times H_i \times W_i}, \qquad (4)$$

where $\sigma(\cdot)$ denotes the ReLU function.

5.2.4 Spatial Reduction

To unify the spatial dimensions, we apply a 3×3 convolution with different stride settings to each feature map. Specifically, strides of $\{8, 4, 2, 1\}$ are used for the four successive stages of the Swin backbone. This design downscales all feature maps to a common resolution of 7×7, while preserving semantic richness (Equation 5).

$$\mathbf{S}_i = \mathrm{BN}\big(\sigma(\mathrm{Conv}_{3\times3,\ \mathrm{stride}=s_i}(\mathbf{F}'_i))\big), \quad \mathbf{S}_i \in \mathbb{R}^{64 \times 7 \times 7}. \quad (5)$$

5.2.5 Feature Fusion

Once channel and spatial dimensions are aligned, as shown in Equation 6 the four feature maps are concatenated along the channel axis:

$$\mathbf{F}_{cat} = \mathrm{Concat}(\mathbf{S}_1, \mathbf{S}_2, \mathbf{S}_3, \mathbf{S}_4), \quad \mathbf{F}_{cat} \in \mathbb{R}^{256 \times 7 \times 7}. \qquad (6)$$

This fusion operation aggregates complementary multi-scale cues, allowing the classifier to benefit simultaneously from low-level structural features and high-level semantic context.

5.2.6 Global Representation

To generate a fixed-dimensional representation invariant to spatial variance, a Global Average Pooling (GAP) layer is applied over $\mathbf{F}_{cat}$, producing a 256-dimensional vector:

$$\mathbf{z} = \mathrm{GAP}(\mathbf{F}_{cat}), \quad \mathbf{z} \in \mathbb{R}^{256}. \qquad (7)$$
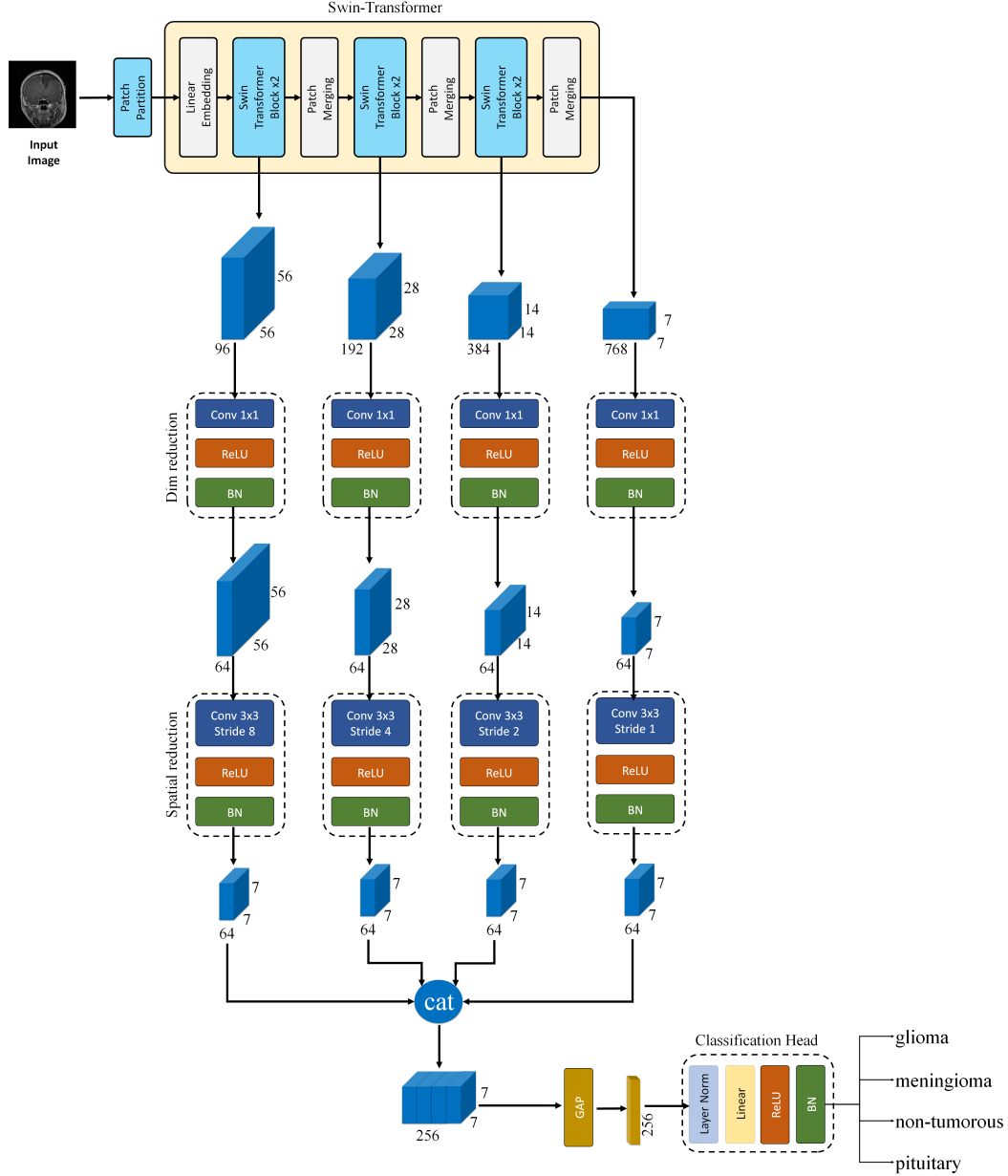
Fig. 11: Overview of the proposed classification module. Multi-scale feature maps from the Swin Transformer backbone are reduced, aligned, fused, and projected into class predictions.

5.2.7 Classification Head

The pooled vector $\mathbf{z}$ is passed through a lightweight classification head composed of Layer Normalization (LN), a fully connected linear projection, ReLU activation, and Batch Normalization:

$$\mathbf{y} = \text{BN}\big(\sigma(\text{Linear}(\text{LN}(\mathbf{z})))\big), \qquad (8)$$

where $\mathbf{y} \in \mathbb{R}^4$ are the class logits. A softmax function is then applied to obtain the final categorical distribution across the four tumor classes.

5.3 Loss Function

To train the proposed segmentation model, we utilize a compound loss function that combines the Binary Cross-Entropy (BCE) loss and the Dice loss. The BCE component focuses on pixel-level classification accuracy, while the Dice loss emphasizes region-level consistency, which is particularly effective in addressing class imbalance commonly present in medical image segmentation tasks.

Given the ground truth mask $y \in \{0,1\}^N$ and the predicted probabilities $\hat{y} \in [0,1]^N$ for N pixels, the BCE loss is formulated as shown in Equation 9.

$$\mathcal{L}_{\text{BCE}} = -\frac{1}{N} \sum_{i=1}^{N} \left[y_i \log(\hat{y}_i) + (1-y_i) \log(1-\hat{y}_i) \right], \qquad (9)$$

The Dice loss, which evaluates the overlap between predicted and ground truth regions, is defined as shown in Equation 10.

$$\mathcal{L}_{\text{Dice}} = 1 - \frac{2 \sum_{i=1}^{N} y_i \hat{y}_i + \epsilon}{\sum_{i=1}^{N} y_i + \sum_{i=1}^{N} \hat{y}_i + \epsilon}, \qquad (10)$$

where ϵ is a small constant added to avoid division by zero.

The final loss used to optimize the network combines these two components, as shown in Equation 11.

$$\mathcal{L}_{\text{total}} = \mathcal{L}_{\text{BCE}} + \mathcal{L}_{\text{Dice}}. \qquad (11)$$

This joint formulation encourages both accurate boundary delineation and robust region-level segmentation.

For the classification task, we adopt the standard Cross-Entropy Loss (CE), which is widely used in multi-class recognition problems due to its effectiveness in penalizing incorrect predictions and encouraging confident probability distributions across classes. The CE loss measures the dissimilarity between the predicted categorical distribution and the ground truth label distribution.

Let C denote the total number of classes, $y \in \{1, \ldots, C\}$ be the ground truth label, and $\hat{p}_c$ be the predicted probability for class c after the softmax activation. The CE loss is defined as:

$$\mathcal{L}_{\text{CE}} = -\sum_{c=1}^{C} \mathbb{1}_{[y=c]} \log(\hat{p}_c), \qquad (12)$$

where $\mathbb{1}_{[y=c]}$ is an indicator function that equals 1 if the true class is c and 0 otherwise. The predicted probabilities are obtained from the logits $\mathbf{y} \in \mathbb{R}^C$ via the softmax function:

$$\hat{p}_c = \frac{\exp(y_c)}{\sum_{j=1}^{C} \exp(y_j)}. \qquad (13)$$

This formulation encourages the network to assign high probability to the correct class while suppressing the probabilities of incorrect classes. Unlike segmentation tasks where pixel-level overlap is a major concern,

classification operates at the image level, making the Cross-Entropy loss a natural and effective choice.

Therefore, the total loss function for the classification branch is expressed as:

$$\mathcal{L}_{\text{classification}} = \mathcal{L}_{\text{CE}}. \qquad (14)$$

6 Technical Validation

Establishing baseline performance is a critical step in evaluating any newly proposed dataset, as it sets a reference point for further research and model development [76]. To validate the effectiveness and versatility of our Brain Tumor MRI Dataset, we conducted experimental evaluations on segmentation and classification tasks.

This section presents a comprehensive analysis of the model used, including their performance metrics, and discusses the implications of these results in the context of the dataset's characteristics and potential applications in medical imaging.

6.1 Evaluation Metrics

6.1.1 Segmentation Metric

In this part, we detail the evaluation metric employed to assess the performance of segmentation models on the proposed dataset. These metrics provide comprehensive insights into the efficacy of the models.

Intersection over Union (IoU) Intersection over Union (IoU), also known as the Jaccard Index, is a fundamental metric for evaluating binary segmentation tasks. It quantifies the overlap between the predicted tumor regions and the ground truth, normalized by their union [77]. For binary segmentation, IoU is computed as shown in Equation 15.

$$\text{IoU} = \frac{\sum_{i=1}^{N} y_i \hat{y}_i}{\sum_{i=1}^{N} y_i + \sum_{i=1}^{N} \hat{y}_i - \sum_{i=1}^{N} y_i \hat{y}_i + \epsilon}, \qquad (15)$$

where $y_i \in \{0,1\}$ denotes the ground truth label, $\hat{y}_i \in \{0,1\}$ represents the predicted label (after thresholding), and ϵ is a small constant added for numerical stability.

As shown in Equation 15, this formulation captures the pixel-wise overlap between the predicted and actual tumor regions and is particularly effective for evaluating segmentation quality, especially along object boundaries.

Table 3: IoU (%) for Brain Tumor Segmentation Models on Different Tumor Types. Weighted mIoU is calculated as a weighted average based on the number of samples per tumor type: Glioma, Meningioma, Pituitary.

Model	mIoU Glioma	mIoU Meningioma	mIoU Pituitary	Weighted mIoU
UNet [64]	69.7	77.1	79.3	75.7
UNet++ [65]	71.7	74.2	79.7	75.3
MANet [66]	72.4	77.5	78.0	76.2
LinkNet [67]	71.7	74.8	79.0	75.3
DeepLabV3+ [68]	72.0	77.5	78.7	76.3
PAN [69]	72.0	74.5	80.7	75.9
EINet [70]	73.6	78.4	80.3	77.7
EU-Net [71]	71.7	76.1	78.3	75.6
DAD [72]	75.2	80.4	82.3	79.5
BASNet [73]	74.0	77.5	81.7	77.9
SaberNet [74]	74.0	82.4	84.3	80.6
ABANet [75]	72.4	80.4	84.7	79.5
Swin-HAFUNet (our)	**76.0**	**85.0**	**85.3**	**82.4**

6.1.2 Classification Metrics

As commonly employed in the evaluation of multi-class classification models, metrics such as Accuracy, Precision, Recall, and F1-Score are widely utilized due to their effectiveness in assessing performance across diverse tasks [78,79,80]. These metrics are defined below to ensure a comprehensive understanding of their applicability to our dataset.

Accuracy Accuracy measures the overall correctness of predictions across all four classes. It is defined as:

$$\text{Accuracy} = \frac{\sum_{i=1}^{C} \text{Correct Predictions for Class } i}{\text{Total Samples}} \quad (16)$$

where C denotes the total number of classes, and "Correct Predictions for Class i" represents the samples correctly classified as class i.

Precision Precision quantifies the proportion of correctly predicted positive instances for each class. For class i, Precision is defined as:

$$\text{Precision}_i = \frac{\text{TP}_i}{\text{TP}_i + \text{FP}_i} \quad (17)$$

In multi-class classification, Precision is averaged using either macro-averaging or weighted-averaging:

$$\text{Macro Precision} = \frac{1}{C} \sum_{i=1}^{C} \text{Precision}_i \quad (18)$$

$$\text{Weighted Precision} = \frac{\sum_{i=1}^{C} w_i \cdot \text{Precision}_i}{\sum_{i=1}^{C} w_i} \quad (19)$$

where w_i represents the proportion of samples in class i.

Recall Recall, or Sensitivity, measures the proportion of actual positive instances correctly identified by the model. For class i, Recall is defined as:

$$\text{Recall}_i = \frac{\text{TP}_i}{\text{TP}_i + \text{FN}_i} \quad (20)$$

For multi-class classification, Recall is averaged similarly to Precision:

$$\text{Macro Recall} = \frac{1}{C} \sum_{i=1}^{C} \text{Recall}_i \quad (21)$$

$$\text{Weighted Recall} = \frac{\sum_{i=1}^{C} w_i \cdot \text{Recall}_i}{\sum_{i=1}^{C} w_i} \quad (22)$$

F1-Score The F1-Score is the harmonic mean of Precision and Recall. For class i, it is defined as:

$$\text{F1-Score}_i = 2 \cdot \frac{\text{Precision}_i \cdot \text{Recall}_i}{\text{Precision}_i + \text{Recall}_i} \tag{23}$$

For multi-class classification, F1-Score is averaged as follows:

$$\text{Macro F1-Score} = \frac{1}{C} \sum_{i=1}^{C} \text{F1-Score}_i \tag{24}$$

$$\text{Weighted F1-Score} = \frac{\sum_{i=1}^{C} w_i \cdot \text{F1-Score}_i}{\sum_{i=1}^{C} w_i} \tag{25}$$

By calculating these metrics per class and aggregating them through macro- or weighted-averaging, we ensure a detailed evaluation of model performance, particularly in datasets with imbalanced class distributions.

6.2 Comparison

6.2.1 Segmentation results

To evaluate the effectiveness of our proposed **Swin-HAFUNet**, we conducted a comparative study against a diverse set of brain tumor segmentation models, including traditional convolutional architectures, attention-enhanced methods, and transformer-based approaches. The baselines include UNet [64], UNet++ [65], LinkNet [67], MANet [66], DeepLabV3+ [68], PAN [69], EINet [70], EU-Net [71], DAD [72], and BASNet [73], as well as two recent transformer-enhanced models, SaberNet [74] and ABANet [75].

Each model was evaluated using the mean Intersection over Union (mIoU) metric for three tumor types: *Glioma*, *Meningioma*, and *Pituitary*. Furthermore, we report a *weighted mIoU*, which is calculated based on the proportion of samples belonging to each tumor type, providing a more representative performance indicator across the dataset.

As summarized in Table 3, our proposed Swin-HAFUNet achieves the highest mIoU scores across all tumor types, particularly excelling in segmenting *Meningioma* and *Pituitary* tumors. It also outperforms all competing methods in terms of weighted mIoU, demonstrating the strength of our architectural design in capturing multi-scale contextual features and handling inter-class variability in medical image segmentation.

In particular, our proposed method achieves the highest weighted mIoU of 82.4%, surpassing the next best-performing model (Saber et al.) by a margin of 2.6%. This improvement underscores the robustness of our approach in handling heterogeneous tumor types. Importantly, the reported weighted mIoU is calculated as a weighted average based on the number of samples in each tumor class to provide a more realistic assessment under dataset imbalance. Unlike simple arithmetic means, the weighted mean better reflects the overall segmentation performance in real-world clinical distributions.

Moreover, our model consistently outperforms existing baselines across all tumor categories, with notable improvements observed in the segmentation of glioma and meningioma tumors. These gains can be attributed to the architectural choices that enhance multi-scale feature extraction and contextual representation, which are particularly beneficial for capturing diverse morphological structures in brain tumors.

It is important to emphasize that the primary goal of this work is to introduce and validate a new brain tumor segmentation dataset, which is designed to support the development of robust and generalizable medical segmentation models. While the proposed method demonstrates promising initial results, we consider this study a foundational step. Future research is expected to build upon this dataset to explore a broader range of models, training protocols, and evaluation settings.

6.2.2 Classification Results

To evaluate the classification performance on our newly introduced brain tumor dataset, we conducted a comprehensive analysis of several baseline models alongside our Proposed Method for classifying brain tumor types: *Glioma*, *Meningioma*, *Pituitary*, and *non-tumorous*. The evaluated models include ResNet50, ResNet101, DenseNet121, DenseNet169, MobileNetV2, MobileNetV3, EfficientNetB0, EfficientNetB1, EfficientNetB2, Xception, VGG16, VGG19, InceptionV3, and our Proposed Method. Each model was trained and tested three times to ensure robust and reliable results, with performance reported as the mean and standard deviation of key metrics: Precision, Recall, F1-Score, and Accuracy.

The evaluation metrics were computed per class, alongside macro and weighted averages, to provide a comprehensive view of model performance across diverse tumor types. The macro average treats all classes equally, while the weighted average accounts for class imbalance by weighting each class's contribution based on the number of samples, offering a realistic assess-

Table 4: Per-Class and Average Classification Performance (%) for Brain Tumor Classification Models. Metrics are reported as mean ± standard deviation over three runs.

Model	Class	Precision	Recall	F1-Score	Accuracy
ResNet50	glioma	0.9868 ± 0.0098	0.9751 ± 0.0164	0.9808 ± 0.0103	-
	meningioma	0.9815 ± 0.0150	0.9673 ± 0.0226	0.9741 ± 0.0087	-
	no_tumor	0.9906 ± 0.0107	0.9952 ± 0.0083	0.9929 ± 0.0035	-
	pituitary	0.9756 ± 0.0285	0.9967 ± 0.0000	0.9859 ± 0.0146	-
	Macro Avg	0.9836 ± 0.0064	0.9836 ± 0.0077	0.9834 ± 0.0072	-
	Weighted Avg	0.9823 ± 0.0076	0.9820 ± 0.0080	0.9820 ± 0.0080	0.9820 ± 0.0080
ResNet101	glioma	0.9726 ± 0.0347	0.9869 ± 0.0082	0.9794 ± 0.0138	-
	meningioma	0.9879 ± 0.0081	0.9575 ± 0.0279	0.9722 ± 0.0106	-
	no_tumor	0.9883 ± 0.0107	0.9905 ± 0.0165	0.9893 ± 0.0037	-
	pituitary	0.9793 ± 0.0113	0.9956 ± 0.0020	0.9874 ± 0.0066	-
	Macro Avg	0.9820 ± 0.0074	0.9826 ± 0.0093	0.9821 ± 0.0086	-
	Weighted Avg	0.9815 ± 0.0085	0.9810 ± 0.0092	0.9810 ± 0.0092	0.9809 ± 0.0092
DenseNet121	glioma	0.4838 ± 0.4753	0.5879 ± 0.5095	0.5197 ± 0.4731	-
	meningioma	0.6640 ± 0.5751	0.2800 ± 0.4569	0.3178 ± 0.4966	-
	no_tumor	0.5324 ± 0.4095	0.6976 ± 0.4871	0.4721 ± 0.4204	-
	pituitary	0.4502 ± 0.4128	0.6422 ± 0.5574	0.5259 ± 0.4678	-
	Macro Avg	0.5326 ± 0.4550	0.5519 ± 0.3376	0.4589 ± 0.4310	-
	Weighted Avg	0.5356 ± 0.4650	0.5253 ± 0.3850	0.5253 ± 0.3850	0.4531 ± 0.4390
DenseNet169	glioma	0.9543 ± 0.0690	0.3543 ± 0.5356	0.3840 ± 0.5173	-
	meningioma	0.7522 ± 0.2090	0.8007 ± 0.2607	0.7560 ± 0.2021	-
	no_tumor	0.4841 ± 0.4507	0.9738 ± 0.0393	0.5754 ± 0.3763	-
	pituitary	0.3333 ± 0.5774	0.3322 ± 0.5754	0.3328 ± 0.5764	-
	Macro Avg	0.6310 ± 0.3116	0.6152 ± 0.3305	0.5121 ± 0.4160	-
	Weighted Avg	0.6404 ± 0.3020	0.5710 ± 0.3689	0.5710 ± 0.3689	0.5093 ± 0.4169
MobileNetV2	glioma	0.3026 ± 0.0558	0.8517 ± 0.1229	0.4418 ± 0.0494	-
	meningioma	0.6667 ± 0.5774	0.0120 ± 0.0180	0.0233 ± 0.0348	-
	no_tumor	0.5343 ± 0.3066	0.6548 ± 0.1750	0.5249 ± 0.0899	-
	pituitary	0.1412 ± 0.2445	0.0400 ± 0.0693	0.0623 ± 0.1080	-
	Macro Avg	0.4112 ± 0.2078	0.3896 ± 0.0345	0.2631 ± 0.0307	-
	Weighted Avg	0.3980 ± 0.2379	0.3237 ± 0.0264	0.3237 ± 0.0264	0.2115 ± 0.0366
MobileNetV3	glioma	0.8912 ± 0.0353	0.9777 ± 0.0082	0.9321 ± 0.0154	-
	meningioma	0.9755 ± 0.0050	0.8639 ± 0.0334	0.9160 ± 0.0175	-
	no_tumor	0.9445 ± 0.0308	1.0000 ± 0.0000	0.9713 ± 0.0165	-
	pituitary	0.9679 ± 0.0073	0.9733 ± 0.0208	0.9706 ± 0.0138	-
	Macro Avg	0.9448 ± 0.0148	0.9537 ± 0.0113	0.9475 ± 0.0140	-
	Weighted Avg	0.9475 ± 0.0123	0.9447 ± 0.0140	0.9447 ± 0.0140	0.9442 ± 0.0142
EfficientNetB0	glioma	0.9960 ± 0.0000	0.9882 ± 0.0000	0.9921 ± 0.0000	-
	meningioma	0.9934 ± 0.0000	0.9869 ± 0.0000	0.9902 ± 0.0000	-
	no_tumor	0.9929 ± 0.0000	1.0000 ± 0.0000	0.9964 ± 0.0000	-
	pituitary	0.9868 ± 0.0000	0.9967 ± 0.0000	0.9917 ± 0.0000	-
	Macro Avg	0.9923 ± 0.0000	0.9929 ± 0.0000	0.9926 ± 0.0000	-
	Weighted Avg	0.9920 ± 0.0000	0.9920 ± 0.0000	0.9920 ± 0.0000	0.9920 ± 0.0000
EfficientNetB1	glioma	0.9987 ± 0.0023	0.9921 ± 0.0000	0.9954 ± 0.0011	-
	meningioma	0.9933 ± 0.0001	0.9750 ± 0.0136	0.9840 ± 0.0070	-
	no_tumor	0.9976 ± 0.0041	1.0000 ± 0.0000	0.9988 ± 0.0021	-
	pituitary	0.9773 ± 0.0116	1.0000 ± 0.0000	0.9885 ± 0.0059	-
	Macro Avg	0.9918 ± 0.0036	0.9918 ± 0.0034	0.9917 ± 0.0036	-
	Weighted Avg	0.9905 ± 0.0040	0.9903 ± 0.0042	0.9903 ± 0.0042	0.9903 ± 0.0042
EfficientNetB2	glioma	0.9919 ± 0.0040	0.9712 ± 0.0164	0.9814 ± 0.0091	-
	meningioma	0.9699 ± 0.0128	0.9782 ± 0.0105	0.9740 ± 0.0084	-
	no_tumor	0.9906 ± 0.0107	1.0000 ± 0.0000	0.9953 ± 0.0054	-
	pituitary	0.9879 ± 0.0082	0.9922 ± 0.0077	0.9900 ± 0.0017	-
	Macro Avg	0.9851 ± 0.0054	0.9854 ± 0.0047	0.9852 ± 0.0051	-
	Weighted Avg	0.9838 ± 0.0049	0.9837 ± 0.0049	0.9837 ± 0.0049	0.9837 ± 0.0049
Xception	glioma	0.0847 ± 0.1466	0.3333 ± 0.5774	0.1350 ± 0.2339	-
	meningioma	0.0000 ± 0.0000	0.0000 ± 0.0000	0.0000 ± 0.0000	-
	no_tumor	0.0933 ± 0.0808	0.6667 ± 0.5774	0.1637 ± 0.1418	-
	pituitary	0.0000 ± 0.0000	0.0000 ± 0.0000	0.0000 ± 0.0000	-
	Macro Avg	0.0445 ± 0.0165	0.2500 ± 0.0000	0.0747 ± 0.0230	-
	Weighted Avg	0.0346 ± 0.0259	0.1780 ± 0.0658	0.1780 ± 0.0658	0.0572 ± 0.0395
VGG16	glioma	0.9803 ± 0.0150	0.9396 ± 0.0741	0.9582 ± 0.0335	-
	meningioma	0.9427 ± 0.0509	0.9684 ± 0.0019	0.9549 ± 0.0257	-
	no_tumor	0.9790 ± 0.0068	0.9976 ± 0.0041	0.9882 ± 0.0020	-
	pituitary	0.9867 ± 0.0099	0.9822 ± 0.0117	0.9844 ± 0.0051	-
	Macro Avg	0.9722 ± 0.0132	0.9720 ± 0.0172	0.9714 ± 0.0162	-
	Weighted Avg	0.9706 ± 0.0157	0.9693 ± 0.0177	0.9693 ± 0.0177	0.9692 ± 0.0178
VGG19	glioma	0.9484 ± 0.0351	0.9541 ± 0.0421	0.9502 ± 0.0081	-
	meningioma	0.9624 ± 0.0130	0.9434 ± 0.0068	0.9527 ± 0.0030	-
	no_tumor	0.9725 ± 0.0231	0.9976 ± 0.0041	0.9848 ± 0.0111	-
	pituitary	0.9744 ± 0.0287	0.9745 ± 0.0267	0.9739 ± 0.0039	-
	Macro Avg	0.9645 ± 0.0061	0.9674 ± 0.0047	0.9654 ± 0.0047	-
	Weighted Avg	0.9639 ± 0.0039	0.9630 ± 0.0044	0.9630 ± 0.0044	0.9629 ± 0.0044
InceptionV3	glioma	0.6564 ± 0.5686	0.5315 ± 0.4983	0.5778 ± 0.5128	-
	meningioma	0.8972 ± 0.1694	0.6645 ± 0.5132	0.6401 ± 0.4458	-
	no_tumor	0.5887 ± 0.4180	0.9905 ± 0.0165	0.6719 ± 0.3794	-
	pituitary	0.6629 ± 0.5741	0.5722 ± 0.5132	0.6104 ± 0.5343	-
	Macro Avg	0.7013 ± 0.3670	0.6897 ± 0.3750	0.6250 ± 0.4676	-
	Weighted Avg	0.7225 ± 0.3490	0.6487 ± 0.4312	0.6487 ± 0.4312	0.6198 ± 0.4797
Proposed method	glioma	0.9974 ± 0.0023	0.9948 ± 0.0023	0.9961 ± 0.0020	-
	meningioma	0.9946 ± 0.0018	0.9945 ± 0.0068	0.9945 ± 0.0025	-
	no_tumor	0.9976 ± 0.0041	1.0000 ± 0.0000	0.9988 ± 0.0021	-
	pituitary	0.9967 ± 0.0033	0.9978 ± 0.0019	0.9972 ± 0.0009	-
	Macro Avg	0.9966 ± 0.0018	0.9968 ± 0.0013	0.9967 ± 0.0016	-
	Weighted Avg	0.9963 ± 0.0015	0.9963 ± 0.0015	0.9963 ± 0.0015	0.9963 ± 0.0015

ment of performance in clinical scenarios where tumor type distributions may vary.

As presented in Table 4, our proposed method achieves the highest overall performance, with a weighted average F1-Score of 0.9963 ± 0.0015 and an accuracy of 0.9963 ± 0.0015, demonstrating exceptional consistency and robustness. Notably, it achieves near-perfect performance across all classes, with an F1-Score of 0.9988 ± 0.0021 for non-tumorous and 0.9961 ± 0.0020 for Glioma, surpassing all baseline models. These gains can be attributed to architectural innovations that enhance multi-scale feature extraction and contextual representation, which are particularly effective for capturing the diverse morphological structures of brain tumors.

Among the baseline models, EfficientNetB0 performs strongly, with a weighted average F1-score of 0.9920 ± 0.0000 and an accuracy of 0.9920 ± 0.0000, achieving perfect recall (1.0000 ± 0.0000) for the *non-tumorous* class. EfficientNetB1 follows closely with a weighted F1-score of 0.9903 ± 0.0042, while ResNet50 and MobileNetV3 deliver competitive results (weighted F1-scores of 0.9820 ± 0.0080 and 0.9447 ± 0.0140, respectively).

In contrast, Xception exhibits the lowest performance, with a weighted F1-score of 0.1780 ± 0.0658, failing entirely on meningioma and pituitary (F1-score: 0.0000 ± 0.0000). Similarly, DenseNet121 and DenseNet169 show unstable performance, with high standard deviations, indicating limited generalizability. MobileNetV2 also struggles, particularly with meningioma (recall: 0.0120 ± 0.0180), likely due to insufficient model capacity.

The VGG variants (VGG16 and VGG19) achieve moderate performance, with weighted F1-scores of 0.9693 ± 0.0177 and 0.9630 ± 0.0044, respectively, while InceptionV3 shows inconsistent results (weighted F1-score: 0.6487 ± 0.4312), reflecting challenges in handling complex tumor morphology or class imbalances.

This evaluation underscores the strong performance of EfficientNet models, particularly EfficientNetB0, which combines high accuracy with remarkable stability across all tumor types. The results validate the utility of our dataset for developing reliable diagnostic tools, while the stark performance differences across architectures emphasize the importance of model selection in medical imaging tasks, where precision and consistency are critical. This work establishes a robust benchmark for brain tumor classification and provides a foundation for future research to explore diverse models and training protocols using this dataset.

6.3 Ablation study

To evaluate the contribution of each component in the proposed Swin-HAFUNet architecture for segmentation task, we conducted an ablation study. Four configurations were tested by progressively integrating the HAF module and the CBE into the baseline. The results are reported in Table 5.

The baseline model includes a simple Swin-UNet structure without the HAF or CBE modules. Adding the HAF module alone leads to a notable improvement across all tumor types, increasing the weighted mIoU from 79.8% to 81.1%. This indicates that the hierarchical attention fusion effectively enhances the representation of skip connections.

Incorporating the CBE module without HAF further improves performance, yielding a weighted mIoU of 81.3%. This demonstrates the benefit of contextual feature extraction and enrichment in the encoder path.

Table 5: The performance of different configuration of Swin-HAFUNet in segmentation task.

baseline	HAF	CBE	mIoU Glioma	mIoU Meningioma	mIoU Pituitary	Weighted mIoU
✓			73.6	82.4	82.3	79.8
✓	✓		75.2	83.5	83.6	81.1
✓		✓	74.4	83.8	84.7	81.3
✓	✓	✓	76.0	85.0	85.3	82.4

Finally, the complete model that includes both HAF and CBE achieves the best performance with a weighted mIoU of 82.4%. The consistent gains across all tumor categories (particularly glioma, which is typically more challenging) highlight the complementary strengths of the proposed components and their combined effectiveness in accurate tumor segmentation.

7 Conclusion

This paper introduces a new, carefully curated brain tumor MRI dataset designed to address critical limitations in existing public datasets, such as class imbalance, lack of tumor diversity, and inconsistent annotations. The dataset includes high-quality T1-weighted contrast-enhanced MRI scans of three major brain tumor types as well as non-tumorous cases, with annotations verified by both radiologists and physicians. With its balanced class distribution and inclusion of multiple imaging planes, the dataset provides a robust foundation for advancing segmentation and classification research in medical imaging. To validate the dataset's utility, we proposed a transformer-based segmentation

model and benchmarked its performance against established baselines. Experimental results demonstrate that our method achieves superior segmentation accuracy, particularly in challenging tumor categories, and highlights the importance of architecture designs that enhance multi-scale and contextual feature representations. Importantly, we employed a weighted mean IoU metric that accounts for class imbalance, offering a more realistic evaluation of model performance. While the proposed model demonstrates promising initial results, it should be noted that the primary contribution of this work lies in the dataset itself. This study represents the beginning of a broader research direction, and we envision that future works will build upon this dataset to explore more sophisticated models, multi-modal imaging integration, and clinically informed evaluation protocols. We aim for this dataset to serve as a benchmark for the community and facilitate the development of accurate and generalizable medical image analysis systems. This study represents the beginning of a broader research direction, and we envision that future works will build upon this dataset to explore more sophisticated models, multi-modal imaging integration, and clinically informed evaluation protocols. In particular, we plan to develop and benchmark advanced classification methods alongside our segmentation approach, evaluating a variety of state-of-the-art architectures to establish comprehensive baselines for tumor type identification. We aim for this dataset to serve as a benchmark for the community and facilitate the development of accurate and generalizable medical image analysis systems.

Data Availability

We introduce a new dataset, BRISC (Brain Tumor MRI Dataset for Segmentation and Classification), which is publicly available at `https://www.kaggle.com/datasets/briscdataset/brisc2025/`.

Code Availability

The custom code developed for the proposed method and the trained models are publicly available at the BRISC dataset repository on Kaggle: `https://www.kaggle.com/datasets/briscdataset/brisc2025/`.

Acknowledgements

Author Contributions

Competing Interests

The authors declare no competing interests.

References

1. L.-K. Ge, P. Gao, D. Chang, J.-J. Nie, Y.-S. Wang, X.-N. Zuo, and G.-X. Wei, "An open data for imaging acute aerobic exercise effects on brain and mind in emerging adulthood," *Scientific Data*, vol. 11, no. 1, p. 1422, 2024.

2. M. Usman Akbar, M. Larsson, I. Blystad, and A. Eklund, "Brain tumor segmentation using synthetic mr images-a comparison of gans and diffusion models," *Scientific Data*, vol. 11, no. 1, p. 259, 2024.

3. Z. Sun, J. Huang, X. Ma, J. Liang, C. Sun, L. Hu, H. He, and G. Yu, "A low-field mri dataset for spatiotemporal analysis of developing brain," *Scientific Data*, vol. 12, no. 1, p. 109, 2025.

4. Q. Zhu, S. Li, Z. Cao, Y. Shen, H. Xu, G. Xu, H. Li, Z. Cui, K. Zhu, Z. Zhao *et al.*, "7 tesla multimodal mri dataset of ex-vivo human brain," *Scientific Data*, vol. 12, no. 1, p. 845, 2025.

5. Z. Gong, T. Xu, N. Peng, X. Cheng, C. Niu, B. Wiestler, F. Hong, and H. B. Li, "A multi-center, multi-parametric mri dataset of primary and secondary brain tumors," *Scientific Data*, vol. 11, no. 1, p. 789, 2024.

6. S. Dorosti, T. Landry, K. Brewer, A. Forbes, C. Davis, and J. Brown, "High-resolution ultrasound data for ai-based segmentation in mouse brain tumor," *Scientific Data*, vol. 12, no. 1, p. 1322, 2025.

7. C. Li, D. Yang, S. Yao, S. Wang, Y. Wu, L. Zhang, Q. Li, K. I. K. Cho, J. Seitz-Holland, L. Ning *et al.*, "Ddevenet: Evidence-based ensemble learning for uncertainty-aware brain parcellation using diffusion mri," *Computerized Medical Imaging and Graphics*, vol. 120, p. 102489, 2025.

8. S. Rezvani, M. Fateh, Y. Jalali, and A. Fateh, "Fusionlungnet: Multi-scale fusion convolution with refinement network for lung ct image segmentation," *Biomedical Signal Processing and Control*, vol. 107, p. 107858, 2025.

9. Q. Zhang, Y. Hang, J. Qiu, and H. Chen, "Application of u-net network utilizing multiattention gate for mri segmentation of brain tumors," *Journal of Computer Assisted Tomography*, vol. 48, no. 6, pp. 991–997, 2024.

10. F. Askari, A. Fateh, and M. R. Mohammadi, "Enhancing few-shot image classification through learnable multi-scale embedding and attention mechanisms," *Neural Networks*, vol. 187, p. 107339, 2025.

11. A. Fateh, M. R. Mohammadi, and M. R. J. Motlagh, "Msdnet: Multi-scale decoder for few-shot semantic segmentation via transformer-guided prototyping," *arXiv preprint arXiv:2409.11316*, 2024.

12. B. H. Menze, A. Jakab, S. Bauer, J. Kalpathy-Cramer, K. Farahani, J. Kirby, Y. Burren, N. Porz, J. Slotboom, R. Wiest *et al.*, "The multimodal brain tumor image segmentation benchmark (brats)," *IEEE transactions on medical imaging*, vol. 34, no. 10, pp. 1993–2024, 2014.

13. J. Cheng, "brain tumor dataset," 4 2017. [Online]. Available: https://figshare.com/articles/dataset/brain_tumor_dataset/1512427

14. M. Ghaffari, A. Sowmya, and R. Oliver, "Automated brain tumor segmentation using multimodal brain scans: a survey based on models submitted to the brats 2012–2018 challenges," *IEEE reviews in biomedical engineering*, vol. 13, pp. 156–168, 2019.

15. D. LaBella, U. Baid, O. Khanna, S. McBurney-Lin, R. McLean, P. Nedelec, A. Rashid, N. H. Tahon, T. Altes, R. Bhalerao *et al.*, "Analysis of the brats 2023 intracranial meningioma segmentation challenge," *arXiv preprint arXiv:2405.09787*, 2024.

16. S. G. De Benedictis, G. Gargano, and G. Settembre, "Enhanced mri brain tumor detection and classification via topological data analysis and low-rank tensor decomposition," *Journal of Computational Mathematics and Data Science*, vol. 13, p. 100103, 2024.

17. S. Sarkar, H. Singh, and J. Chawla, "Evolution of lung tumor segmentation: Comprehensive analysis," in *2024 International Conference on Advances in Computing, Communication and Applied Informatics (ACCAI)*. IEEE, 2024, pp. 1–7.

18. H. R. Khajeha, M. Fateh, V. Abolghasemi, A. R. Fateh, M. H. Emamian, H. Hashemi, and A. Fotouhi, "Advancing glaucoma diagnosis through multi-scale feature extraction and cross-attention mechanisms in optical coherence tomography images," *Engineering Reports*, vol. 7, no. 4, p. e70110, 2025.

19. M. S. Fakhima, M. Fateh, A. Fateh, and Y. Jalalia, "Dacovsgnet: Double attentional network for covid severity grading," *International Journal of Engineering, Transactions A: Basics*, vol. 38, no. 07, pp. 1568–82, 2025.

20. S. Rezvani, F. S. Siahkar, Y. Rezvani, A. A. Gharahbagh, and V. Abolghasemi, "Single image denoising via a new lightweight learning-based model," *IEEE Access*, 2024.

21. M. C. de Verdier, R. Saluja, L. Gagnon, D. LaBella, U. Baid, N. H. Tahon, M. Foltyn-Dumitru, J. Zhang, M. Alafif, S. Baig *et al.*, "The 2024 brain tumor segmentation (brats) challenge: Glioma segmentation on post-treatment mri," *arXiv preprint arXiv:2405.18368*, 2024.

22. M. Antonelli, A. Reinke, S. Bakas, K. Farahani, A. Kopp-Schneider, B. A. Landman, G. Litjens, B. Menze, O. Ronneberger, R. M. Summers *et al.*, "The medical segmentation decathlon," *Nature communications*, vol. 13, no. 1, p. 4128, 2022.

23. S. Pati, U. Baid, M. Zenk, B. Edwards, M. Sheller, G. A. Reina, P. Foley, A. Gruzdev, J. Martin, S. Albarqouni *et al.*, "The federated tumor segmentation (fets) challenge," *arXiv preprint arXiv:2105.05874*, 2021.

24. S. C. for Artificial Intelligence in Medicine & Imaging, "Brainmetshare dataset," 2021, a brain MRI dataset to develop and test improved methods for detection and segmentation of brain metastases. [Online]. Available: https://doi.org/10.71718/z66c-qr59

25. D. S. Marcus, T. H. Wang, J. Parker, J. G. Csernansky, J. C. Morris, and R. L. Buckner, "Open access series of imaging studies (oasis)," 2007, a project aimed at making neuroimaging datasets of the brain freely available to the scientific community. [Online]. Available: https://www.oasis-brains.org/

26. J. Zbontar, F. Knoll, A. Sriram, T. Murrell, Z. Huang, M. J. Muckley, A. Defazio, R. Stern, P. Johnson, M. Bruno, M. Parente, K. J. Geras, J. Katsnelson, H. Chandarana, Z. Zhang, M. Drozdzal, A. Romero, M. Rabbat, P. Vincent, N. Yakubova, E. Owens, C. L. Zitnick, M. P. Recht, D. K. Sodickson, and L. Pineda, "fastmri dataset," 2018, a large-scale dataset of both raw MRI measurements and clinical DICOM images for advancing machine learning research in medical imaging. [Online]. Available: https://fastmri.med.nyu.edu/

27. M. Buda, A. Saha, and M. A. Mazurowski, "Lgg mri segmentation dataset," 2019, brain MRI images together with manual FLAIR abnormality segmentation masks. [Online]. Available: https://www.kaggle.com/datasets/mateuszbuda/lgg-mri-segmentation

28. M. M. Islam, M. A. Talukder, M. A. Uddin, A. Akhter, and M. Khalid, "Brainnet: precision brain tumor classification with optimized efficientnet architecture," *International Journal of Intelligent Systems*, vol. 2024, no. 1, p. 3583612, 2024.

29. B. AG, S. Srinivasan, M. P, S. K. Mathivanan, and M. A. Shah, "Robust brain tumor classification by fusion of deep learning and channel-wise attention mode approach," *BMC Medical Imaging*, vol. 24, no. 1, p. 147, 2024.

30. M. Nickparvar, "Brain tumor mri dataset," 2021. [Online]. Available: https://www.kaggle.com/datasets/masoudnickparvar/brain-tumor-mri-dataset

31. W. Chen, X. Tan, J. Zhang, G. Du, Q. Fu, and H. Jiang, "A robust approach for multi-type classification of brain tumor using deep feature fusion," *Frontiers in Neuroscience*, vol. 18, p. 1288274, 2024.

32. M. F. Alanazi, M. U. Ali, S. J. Hussain, A. Zafar, M. Mohatram, M. Irfan, R. AlRuwaili, M. Alruwaili, N. H. Ali, and A. M. Albarrak, "Brain tumor/mass classification framework using magnetic-resonance-imaging-based isolated and developed transfer deep-learning model," *Sensors*, vol. 22, no. 1, p. 372, 2022.

33. P. Ghosal, L. Nandanwar, S. Kanchan, A. Bhadra, J. Chakraborty, and D. Nandi, "Brain tumor classification using resnet-101 based squeeze and excitation deep neural network," in *2019 Second International Conference on Advanced Computational and Communication Paradigms (ICACCP)*. IEEE, 2019, pp. 1–6.

34. F. Gaillard, T. Walizai, R. Sharma, and et al., "Brain tumors," 2024. [Online]. Available: https://doi.org/10.53347/rID-4986

35. K. Aldape, K. M. Brindle, L. Chesler, R. Chopra, A. Gajjar, M. R. Gilbert, N. Gottardo, D. H. Gutmann, D. Hargrave, E. C. Holland *et al.*, "Challenges to curing primary brain tumours," *Nature reviews Clinical oncology*, vol. 16, no. 8, pp. 509–520, 2019.

36. E. M. Senan, M. E. Jadhav, T. H. Rassem, A. S. Aljaloud, B. A. Mohammed, and Z. G. Al-Mekhlafi, "Early diagnosis of brain tumour mri images using hybrid techniques between deep and machine learning," *Computational and*

Mathematical Methods in Medicine, vol. 2022, no. 1, p. 8330833, 2022.

37. S. Lapointe, A. Perry, and N. A. Butowski, "Primary brain tumours in adults," *The Lancet*, vol. 392, no. 10145, pp. 432–446, 2018.

38. S. Sunaert, "Presurgical planning for tumor resectioning," *Journal of Magnetic Resonance Imaging: An Official Journal of the International Society for Magnetic Resonance in Medicine*, vol. 23, no. 6, pp. 887–905, 2006.

39. A. Fateh, M. Rezvani, A. Tajary, and M. Fateh, "Providing a voting-based method for combining deep neural network outputs to layout analysis of printed documents," *Journal of Machine Vision and Image Processing*, vol. 9, no. 1, pp. 47–64, 2022.

40. A. Mehndiratta and F. L. Giesel, *Brain tumour imaging.* INTECH Open Access Publisher, 2011.

41. A. Perry and P. Wesseling, "Histologic classification of gliomas," *Handbook of clinical neurology*, vol. 134, pp. 71–95, 2016.

42. K. R. Jessen, "Glial cells," *The international journal of biochemistry & cell biology*.

43. A.-R. Fathi and U. Roelcke, "Meningioma," *Current neurology and neuroscience reports*, vol. 13, pp. 1–8, 2013.

44. K. Dasgupta and J. Jeong, "Developmental biology of the meninges," *genesis*, vol. 57, no. 5, p. e23288, 2019.

45. C. Marosi, M. Hassler, K. Roessler, M. Reni, M. Sant, E. Mazza, and C. Vecht, "Meningioma," *Critical reviews in oncology/hematology*, vol. 67, no. 2, pp. 153–171, 2008.

46. P.-F. Yan, L. Yan, T.-T. Hu, D.-D. Xiao, Z. Zhang, H.-Y. Zhao, and J. Feng, "The potential value of preoperative mri texture and shape analysis in grading meningiomas: a preliminary investigation," *Translational oncology*, vol. 10, no. 4, pp. 570–577, 2017.

47. R. E. Bancalari, L. C. Gregory, M. J. McCabe, and M. T. Dattani, "Pituitary gland development: an update," *Endocr Dev*, vol. 23, no. 1, 2012.

48. S. L. Asa and S. Ezzat, "The pathogenesis of pituitary tumours," *Nature Reviews Cancer*, vol. 2, no. 11, pp. 836–849, 2002.

49. G. Raverot, M. D. Ilie, H. Lasolle, V. Amodru, J. Trouillas, F. Castinetti, and T. Brue, "Aggressive pituitary tumours and pituitary carcinomas," *Nature Reviews Endocrinology*, vol. 17, no. 11, pp. 671–684, 2021.

50. A. Kelly, "Neurological therapeutics: Principles andpractice, secondedition," 2008.

51. A. Reang, "Clinico-radiologic profile of intracranial space occupying lesion imaged with mri and spectroscopy in a tertiary care centre," *International Journal of Life Sciences, Biotechnology and Pharma Research*, vol. 14, 2025.

52. Kenhub, "Anatomical terminology: Planes, directions & regions," 2025, accessed: 2025-05-31. [Online]. Available: https://www.kenhub.com/en/library/anatomy/anatomical-terminology

53. C. Westbrook and J. Talbot, *MRI in Practice.* John Wiley & Sons, 2018.

54. G. Katti, S. A. Ara, and A. Shireen, "Magnetic resonance imaging (mri)–a review," *International journal of dental clinics*, vol. 3, no. 1, pp. 65–70, 2011.

55. J. Faehndrich, S. Weidauer, U. Pilatus, A. Oszvald, F. Zanella, and E. Hattingen, "Neuroradiological viewpoint on the diagnostics of space-occupying brain lesions," *Clinical neuroradiology*, vol. 21, no. 3, p. 123, 2011.

56. M. Martucci, R. Russo, F. Schimperna, G. D'Apolito, M. Panfili, A. Grimaldi, A. Perna, A. M. Ferranti, G. Varcasia, C. Giordano *et al.*, "Magnetic resonance imaging of primary adult brain tumors: state of the art and future perspectives," *Biomedicines*, vol. 11, no. 2, p. 364, 2023.

57. A. M. Omuro, C. C. Leite, K. Mokhtari, and J.-Y. Delattre, "Pitfalls in the diagnosis of brain tumours," *The Lancet Neurology*, vol. 5, no. 11, pp. 937–948, 2006.

58. P.-F. Yan, L. Yan, Z. Zhang, A. Salim, L. Wang, T.-T. Hu, and H.-Y. Zhao, "Accuracy of conventional mri for preoperative diagnosis of intracranial tumors: A retrospective cohort study of 762 cases," *International Journal of Surgery*, vol. 36, pp. 109–117, 2016.

59. M. Nickparvar, "Brain tumor mri dataset," Kaggle Dataset, 2021, https://www.kaggle.com/datasets/masoudnickparvar/brain-tumor-mri-dataset.

60. S. Bhuvaji, A. Kadam, P. Bhumkar, and S. Dedge, "Brain tumor classification (mri)," Kaggle Dataset, 2021, https://www.kaggle.com/datasets/sartajbhuvaji/brain-tumor-classification-mri.

61. A. Hamada, "Br35h :: Brain tumor detection 2020," Kaggle Dataset, 2020, https://www.kaggle.com/datasets/ahmedhamada0/brain-tumor-detection?select=no.

62. V. Nguyen, "Anylabeling-effortless data labeling with ai support," 2024.

63. J. M. J. Valanarasu and V. M. Patel, "Unext: Mlp-based rapid medical image segmentation network," in *International conference on medical image computing and computer-assisted intervention.* Springer, 2022, pp. 23–33.

64. O. Ronneberger, P. Fischer, and T. Brox, "U-net: Convolutional networks for biomedical image segmentation," in *Medical image computing and computer-assisted intervention–MICCAI 2015: 18th international conference, Munich, Germany, October 5-9, 2015, proceedings, part III 18.* Springer, 2015, pp. 234–241.

65. Z. Zhou, M. M. Rahman Siddiquee, N. Tajbakhsh, and J. Liang, "Unet++: A nested u-net architecture for medical image segmentation," in *Deep learning in medical image analysis and multimodal learning for clinical decision support: 4th international workshop, DLMIA 2018, and 8th international workshop, ML-CDS 2018, held in conjunction with MICCAI 2018, Granada, Spain, September 20, 2018, proceedings 4.* Springer, 2018, pp. 3–11.

66. T. Fan, G. Wang, Y. Li, and H. Wang, "Ma-net: A multi-scale attention network for liver and tumor segmentation," *IEEE Access*, vol. 8, pp. 179 656–179 665, 2020.

67. A. Chaurasia and E. Culurciello, "Linknet: Exploiting encoder representations for efficient semantic segmentation," in *2017 IEEE visual communications and image processing (VCIP).* IEEE, 2017, pp. 1–4.

68. L.-C. Chen, Y. Zhu, G. Papandreou, F. Schroff, and H. Adam, "Encoder-decoder with atrous separable convolution for semantic image segmentation," in *Proceedings of the European conference on computer vision (ECCV)*, 2018, pp. 801–818.

69. H. Li, P. Xiong, J. An, and L. Wang, "Pyramid attention network for semantic segmentation," *arXiv preprint arXiv:1805.10180*, 2018.

70. C. Li and G. Jiao, "Einet: camouflaged object detection with pyramid vision transformer," *Journal of Electronic Imaging*, vol. 31, no. 5, pp. 053 002–053 002, 2022.

71. K. Patel, A. M. Bur, and G. Wang, "Enhanced u-net: A feature enhancement network for polyp segmentation," in *2021 18th conference on robots and vision (CRV).* IEEE, 2021, pp. 181–188.

72. J. Li, W. He, and H. Zhang, "Towards complex backgrounds: A unified difference-aware decoder for binary segmentation," *arXiv preprint arXiv:2210.15156*, 2022.

73. X. Qin, D.-P. Fan, C. Huang, C. Diagne, Z. Zhang, A. C. Sant'Anna, A. Suarez, M. Jagersand, and L. Shao, "Boundary-aware segmentation network for mobile and web applications," *arXiv preprint arXiv:2101.04704*, 2021.

74. A. Saber, P. Parhami, A. Siahkarzadeh, M. Fateh, and A. Fateh, "Efficient and accurate pneumonia detection using a novel multi-scale transformer approach," *arXiv preprint arXiv:2408.04290*, 2024.

75. S. Rezvani, M. Fateh, and H. Khosravi, "Abanet: Attention boundary-aware network for image segmentation," *Expert Systems*, vol. 41, no. 9, p. e13625, 2024.

76. J. Cheng, B. Fu, J. Ye, G. Wang, T. Li, H. Wang, R. Li, H. Yao, J. Chen, J. Li *et al.*, "Interactive medical image segmentation: A benchmark dataset and baseline," *arXiv preprint arXiv:2411.12814*, 2024.

77. H. Rezatofighi, N. Tsoi, J. Gwak, A. Sadeghian, I. Reid, and S. Savarese, "Generalized intersection over union: A metric and a loss for bounding box regression," in *Proceedings of the IEEE/CVF conference on computer vision and pattern recognition*, 2019, pp. 658–666.

78. I. Goodfellow, "Deep learning," 2016.

79. K. He, X. Zhang, S. Ren, and J. Sun, "Deep residual learning for image recognition," in *Proceedings of the IEEE conference on computer vision and pattern recognition*, 2016, pp. 770–778.

80. A. Dosovitskiy, "An image is worth 16x16 words: Transformers for image recognition at scale," *arXiv preprint arXiv:2010.11929*, 2020.